

# Supplementary Information for In Situ Generation of (Sub)Nanometer Pores in MoS<sub>2</sub> Membranes for Ion Selective Transport

Eli Hoenig<sup>1</sup>, Yu Han<sup>1</sup>, Kangli Xu<sup>1</sup>, Jingyi Li<sup>1</sup>, Mingzhan Wang<sup>1</sup>, Chong Liu<sup>1,\*</sup>

<sup>1</sup> Pritzker School of Molecular Engineering, University of Chicago, Chicago, Illinois 60637, United States

\* Correspondence: chongliu@uchicago.edu

**This file includes**

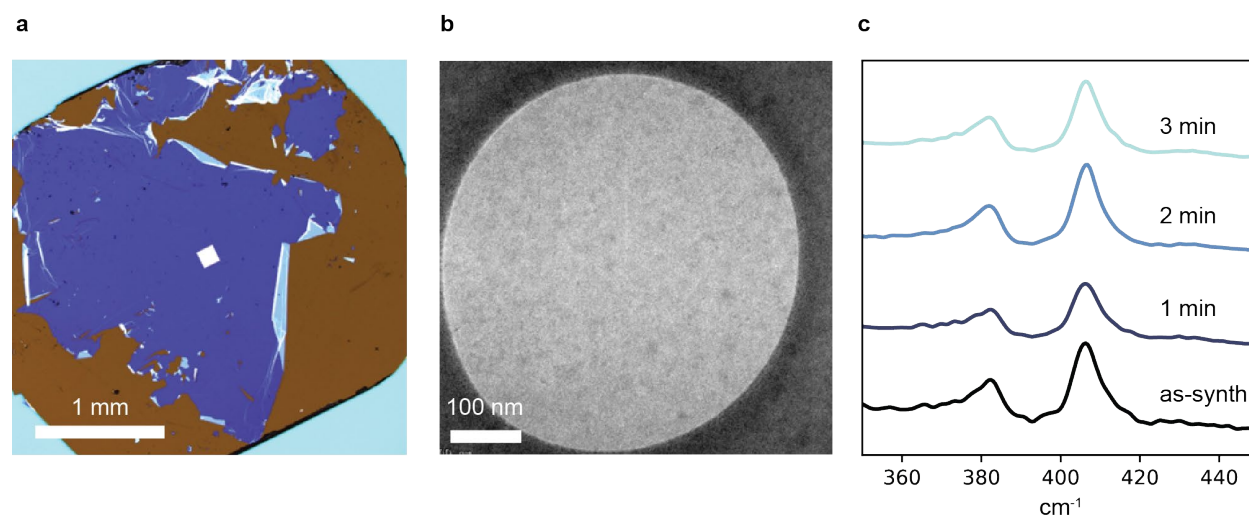
**Supplementary Figures 1-27**

**Supplementary Tables 1-5**

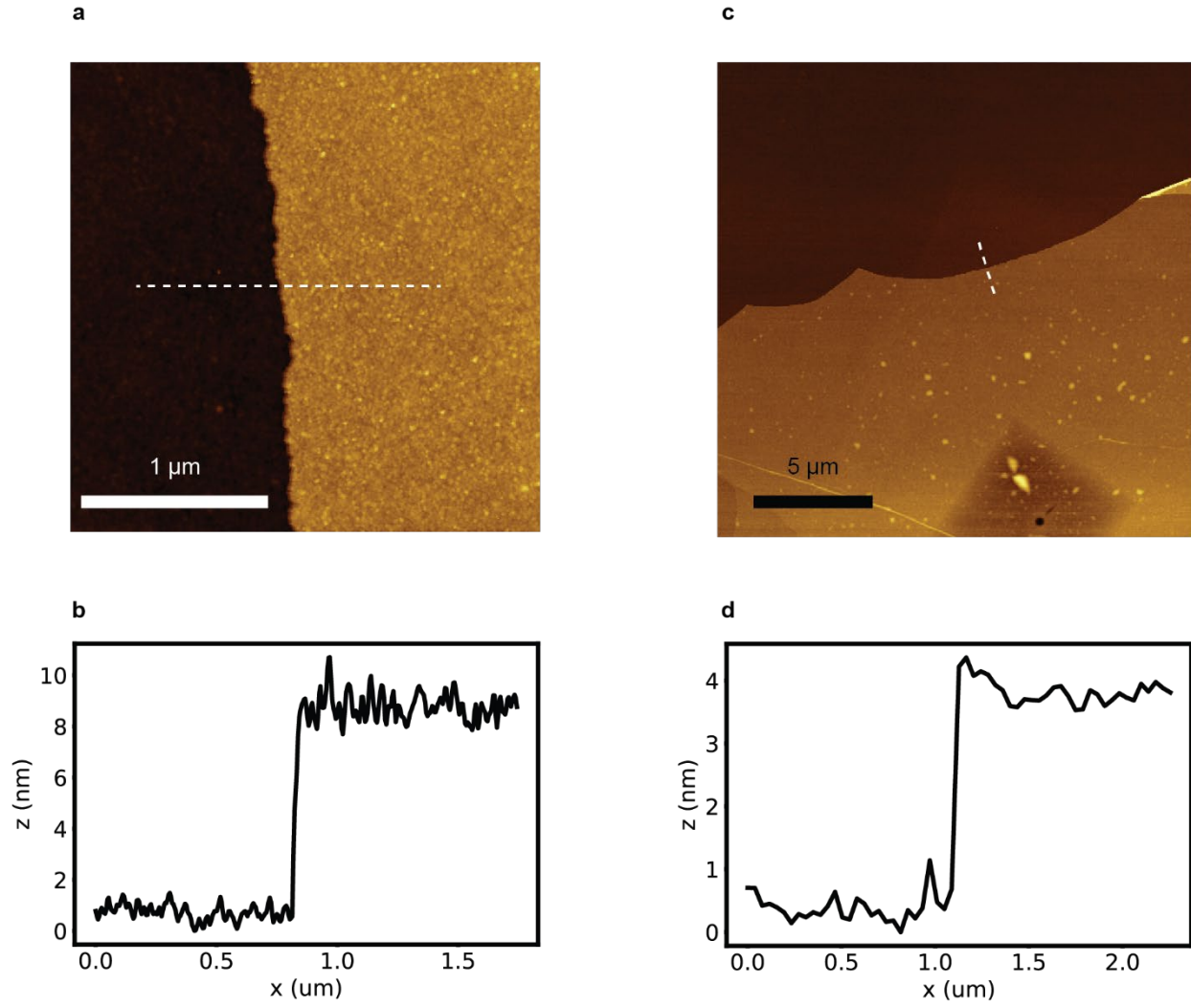
**Supplementary Notes**

**Supplementary Methods**

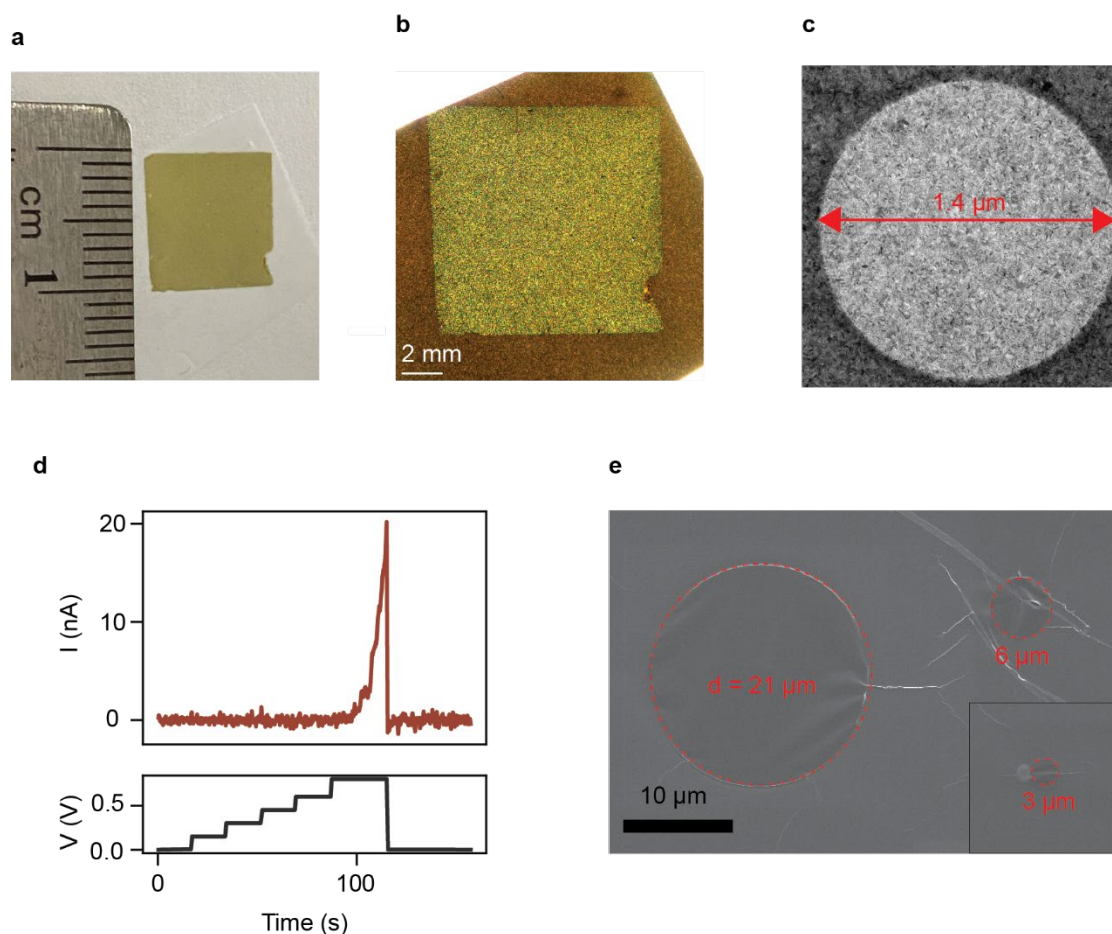
## Supplementary Figures



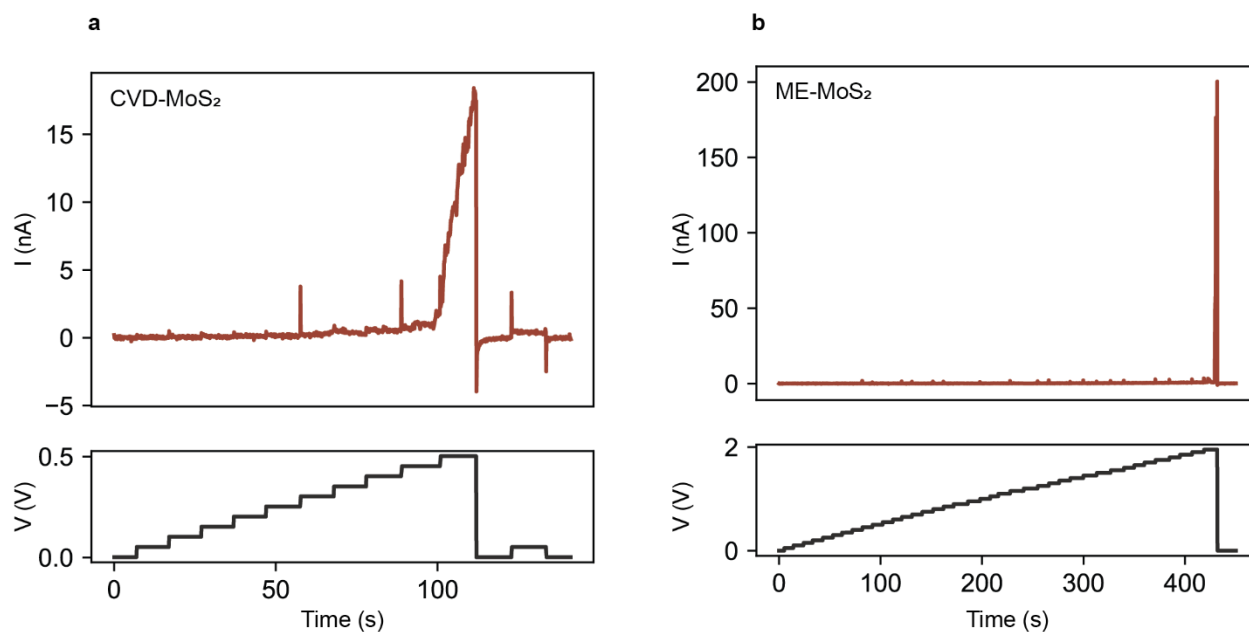
**Supplementary Fig. 1. Transfer and plasma treatment of CVD-MoS<sub>2</sub> on a SiN chip.** (a) Image of a 3 mm SiN TEM grid with a single SiN membrane (white square) in the center. CVD-MoS<sub>2</sub> (blue film) is transferred on the chip and covers the entire SiN membrane. (b) TEM image of CVD-MoS<sub>2</sub> transferred on a single pore drilled in the SiN window. (c) Raman spectra after remote O<sub>2</sub> plasma treatment of CVD-MoS<sub>2</sub>, showing little change in the film integrity. Likely only the first layer of MoS<sub>2</sub> is oxidized<sup>1</sup>.



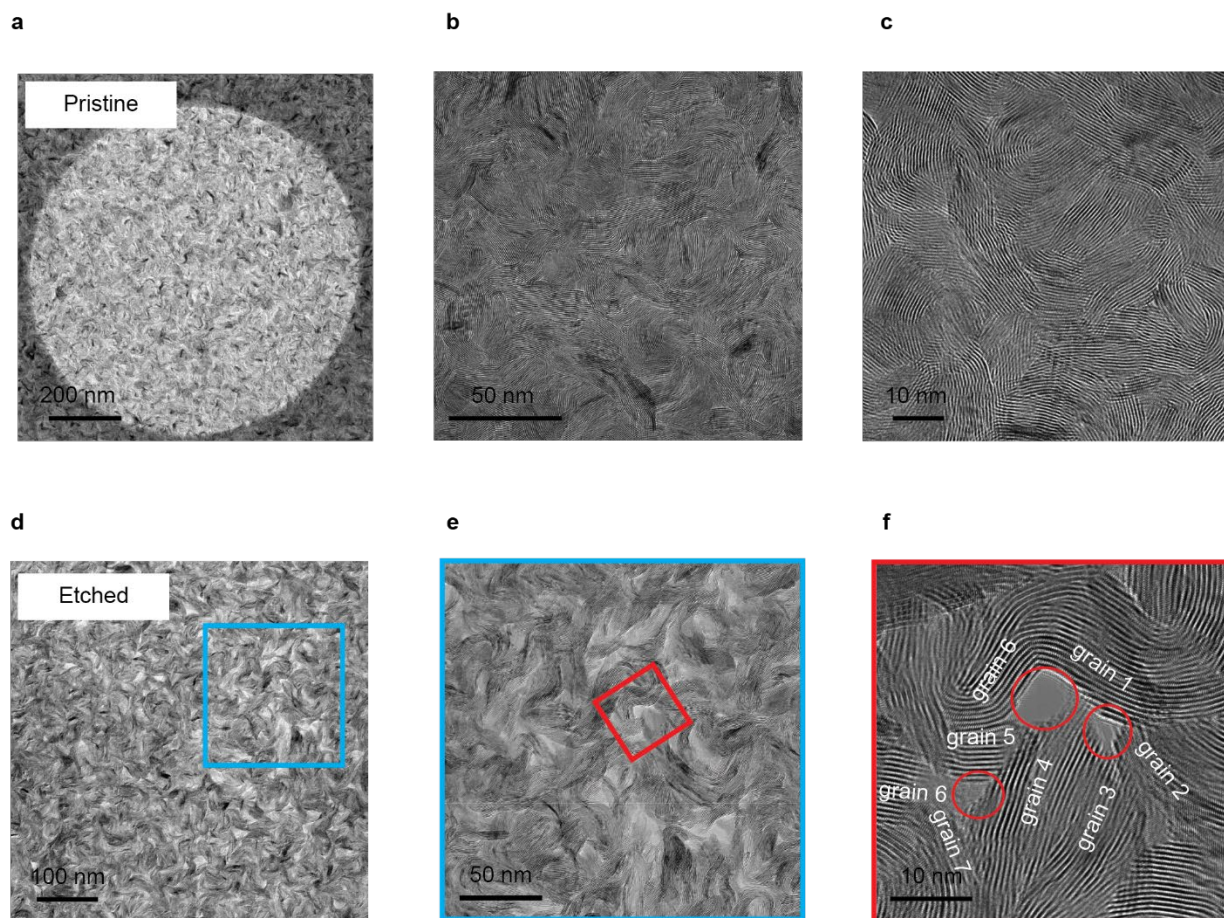
**Supplementary Fig. 2. AFM images of MoS<sub>2</sub> films.** (a) CVD-MoS<sub>2</sub> on SiO<sub>2</sub>, with the corresponding height trace in (b). (c) ME-MoS<sub>2</sub> transferred on a SiN chip, with height trace in (d). Based on these thickness measurements, we infer that the ME-MoS<sub>2</sub> film is five layers thick, and the CVD-MoS<sub>2</sub> film is ~10 layers thick and significantly rougher.



**Supplementary Fig. 3. Demonstration of large-area transfer of CVD-MoS<sub>2</sub>.** MoS<sub>2</sub> is grown on cm-scale SiO<sub>2</sub> coupons; the entirety of these films can be transferred to arbitrary substrates, and pores can be fabricated over micron-scale apertures. (a) cm-scale CVD-MoS<sub>2</sub> on track etched polycarbonate films, with ruler for scale. (b) Optical microscope image of the same film, to show continuity. (c) TEM image of a CVD-MoS<sub>2</sub> film (15 nm Mo seed thickness), after electrochemical pore creation, suspended over a micron-scale aperture. (d) IV trace of pore in c, showing typical pore creation behavior in CVD-MoS<sub>2</sub> films. (e) CVD-MoS<sub>2</sub> films transferred to SiN substrates with a variety of apertures. Due to the superiority of the mechanical properties of 2D materials, CVD-MoS<sub>2</sub>, despite its nanometer-scale thickness and high density of grain boundaries, can be suspended freely over apertures from < 1 to at least 20 μm.

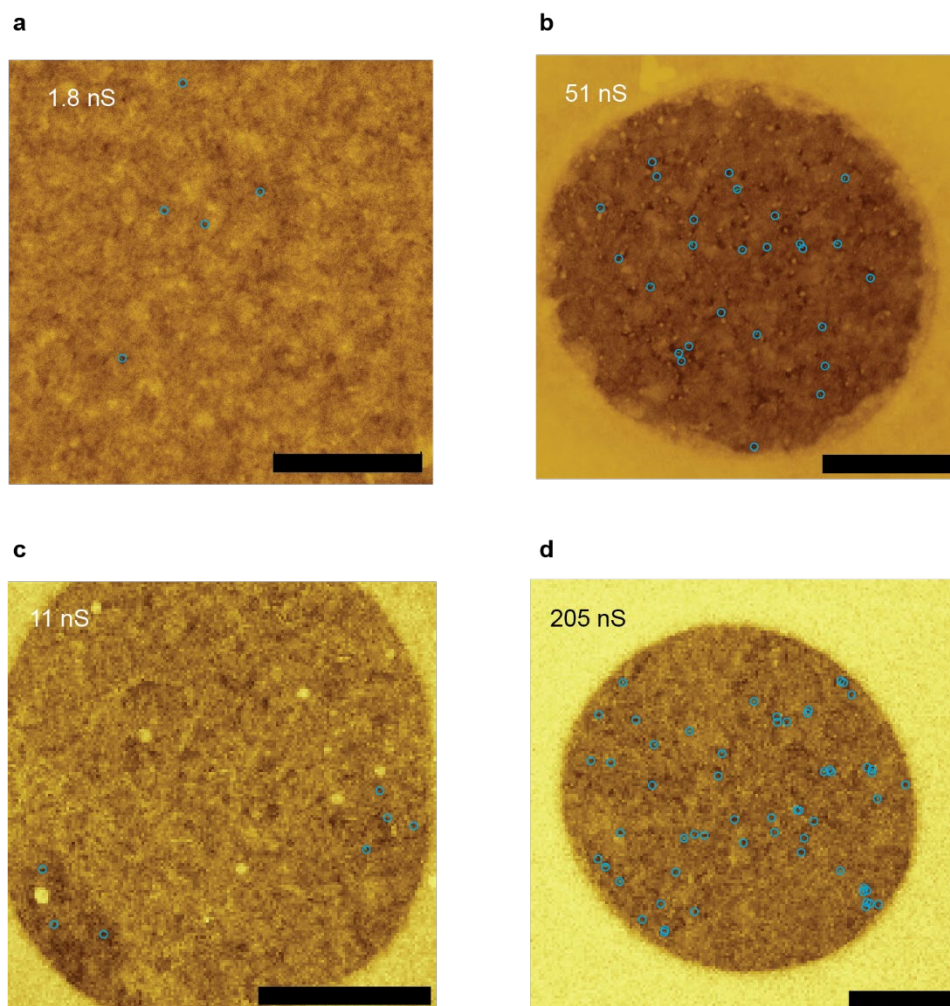


**Supplementary Fig. 4. Electrochemical pore creation in MoS<sub>2</sub> films.** Current and voltage vs time traces depicting electrochemical pore creation in (a) CVD-MoS<sub>2</sub> and (b) ME-MoS<sub>2</sub>. Negligible leakage current is detected for CVD-MoS<sub>2</sub> before the breakdown threshold of 0.4-0.5 V, at which point the current increases rapidly. For ME-MoS<sub>2</sub>, that threshold is pushed to nearly 2 V, and the current increases significantly more rapidly (**Fig. 1**, main text).

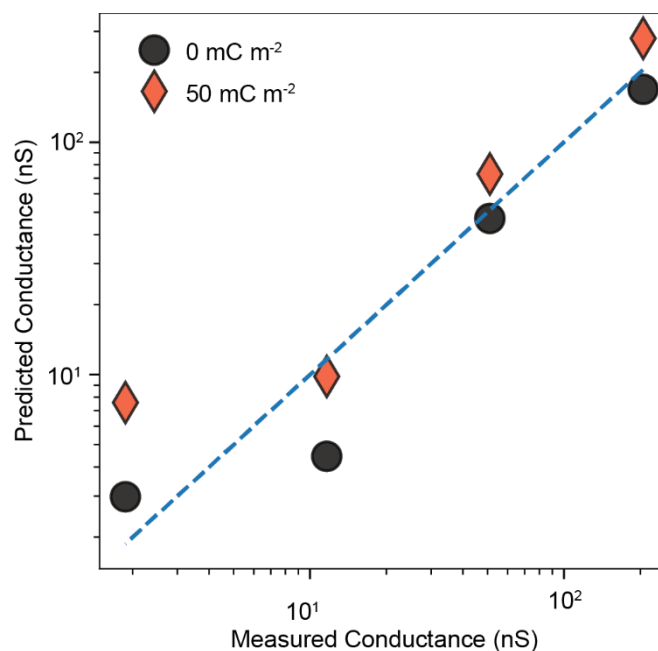


**Supplementary Fig. 5. Pore generation at grain boundaries in vertically aligned MoS<sub>2</sub>.** Here we show vertically aligned MoS<sub>2</sub> before and after electrochemical pore creation. In the pristine sample (a-c) grains are easily visualized by observing the relative orientation of the MoS<sub>2</sub> layers; such visualization is significantly more difficult in horizontally aligned MoS<sub>2</sub>. No discernable gaps or pores are visible between grains. After applying a 1.5 V bias across the membrane for 10 ms in 1 M KCl, the film partially degrades, with pores opening up at the intersections of neighboring grains (d-f). In f, grains are labelled based on the relative orientation of the vertically aligned layers, and pores are circled in red.





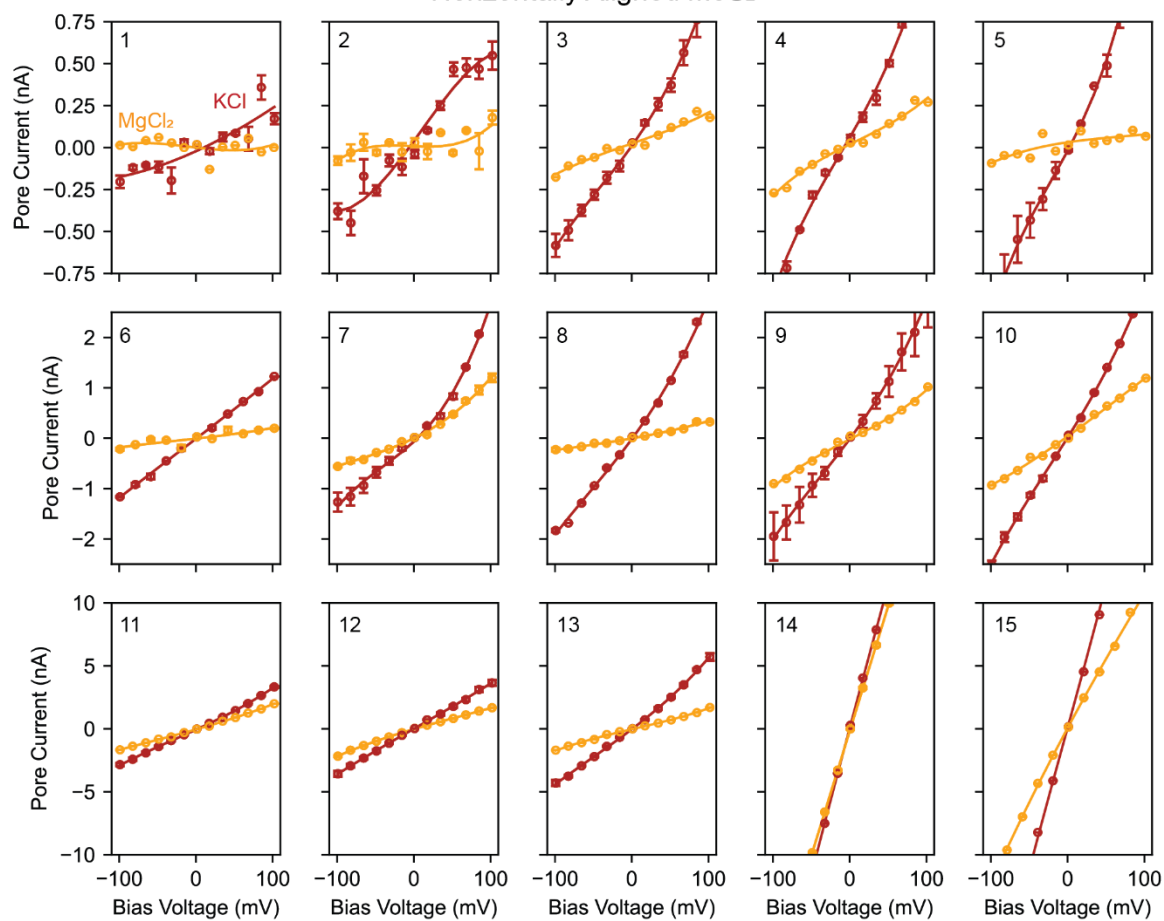
**Supplementary Fig. 6. STEM images of CVD-MoS<sub>2</sub> suspended over SiN pores.** Corresponding ionic conductance, given in top left corners, are measured in 1M KCl, with **(a-d)** listed with increasing ion conductance. The pore size distribution (Fig. 2 in the main text) is determined by the segmentation function implemented in Gwyddion 2.60<sup>2</sup>. The resulting distribution depends on the threshold as well as the degree of Gaussian smoothing. To accurately set these parameters, we tune them until the size of a few select pores match their high-resolution STEM counterparts, as shown for example in Fig. 2 b-c and e-f of the main text. Identified pores are circled. The scale bars in all images are 100 nm.



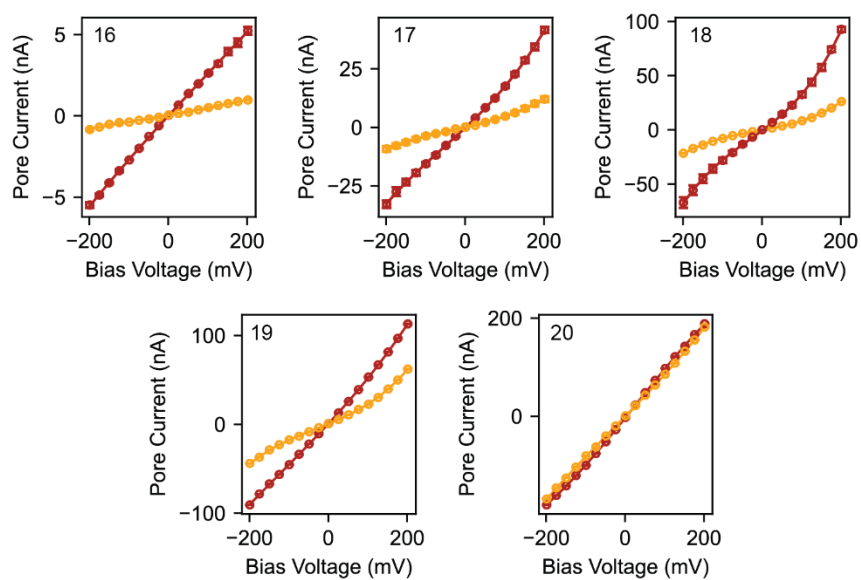
**Supplementary Fig. 7. Predicted conductance vs expected conductance for nanoporous MoS<sub>2</sub> membranes.** Values are calculated from the pore size distribution shown in Fig. 2 h of the main text and using Eq. (5) for both 0 and 50 mC m<sup>-2</sup> against the measured conductance in 1 M KCl. Dashed blue line indicates perfect agreement. Good agreement is observed for the larger pore size distributions; at small pore sizes, the estimation technique begins to diverge from the measured values, likely because the size of a single pixel approaches the size of the nanopores.



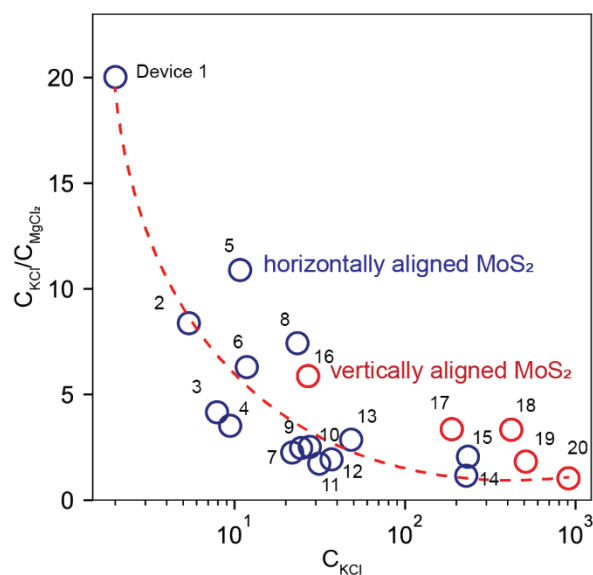
### Horizontally Aligned MoS<sub>2</sub>



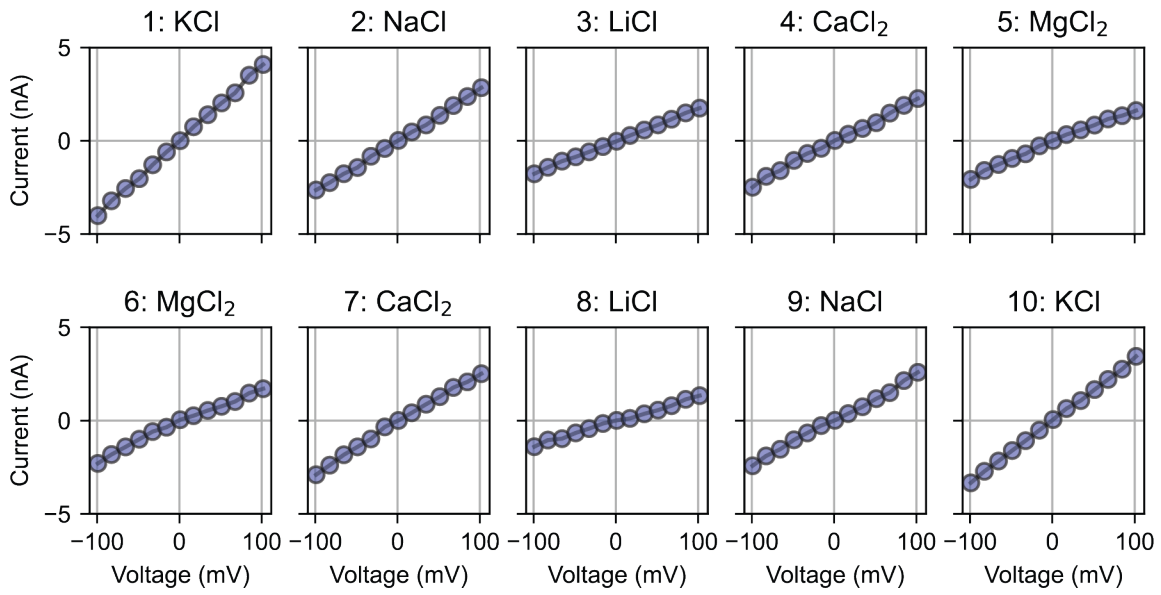
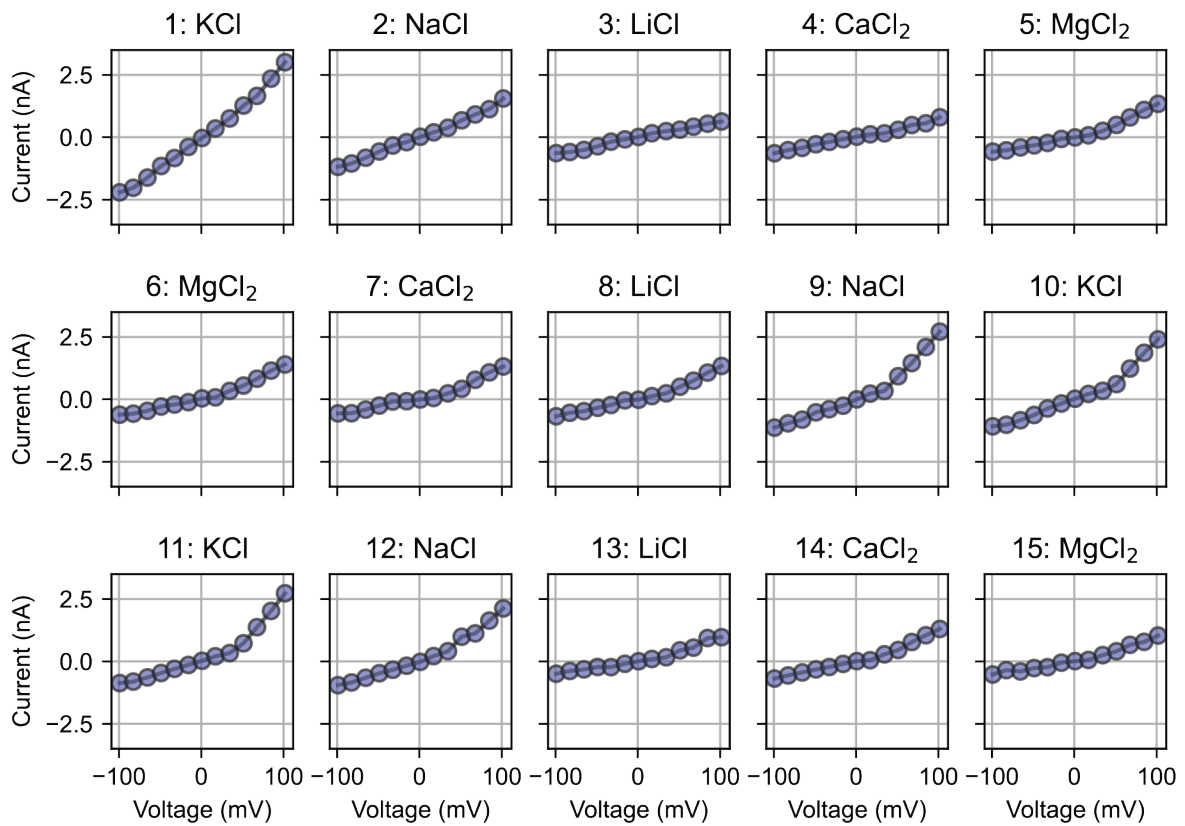
### Vertically Aligned MoS<sub>2</sub>



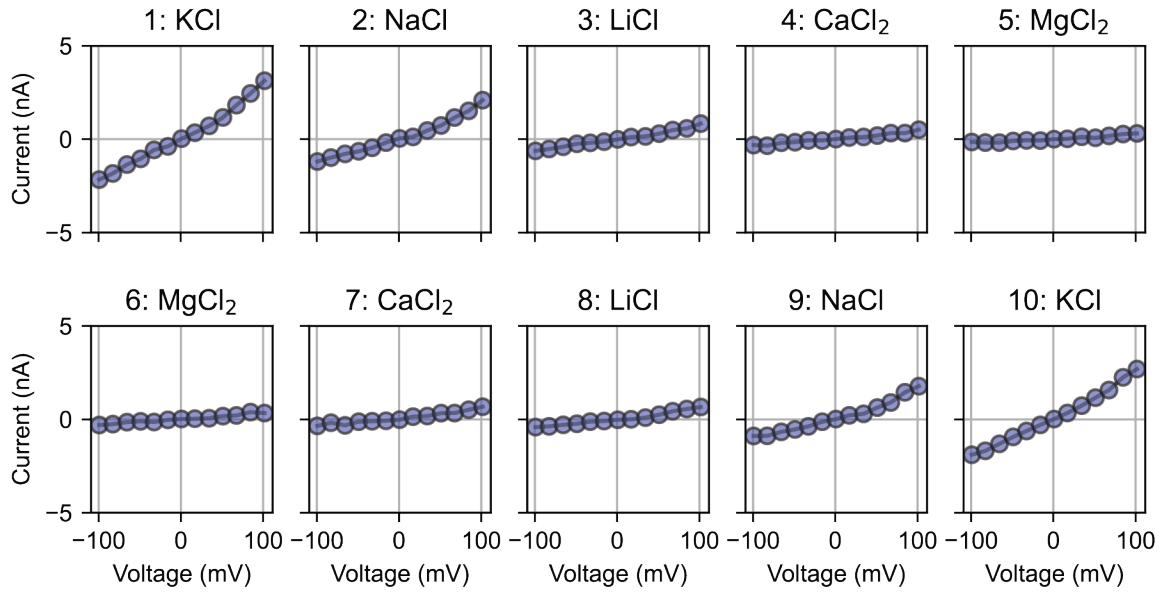
**Supplementary Fig. 8. I-V traces of KCl and MgCl<sub>2</sub> salts in CVD-MoS<sub>2</sub> nanoporous films.** These data correspond to the 15 devices shown in Fig. 3 a (all horizontally aligned MoS<sub>2</sub> films tested for KCl and MgCl<sub>2</sub> selectivity), as well as the 5 vertically aligned devices (> 10 nm Mo seed thickness), displayed all together, in Supplementary Fig. 9. Details for each device are tabulated in Supplementary Table 1. Data are collected using 1 M salts, except for devices 16, 18, 19 and 20, which were collected with 0.1 M salts. The current shown for these devices has been scaled by a factor of 10 to correct for this difference. Error bars correspond to the standard error of multiple traces (N>=3).



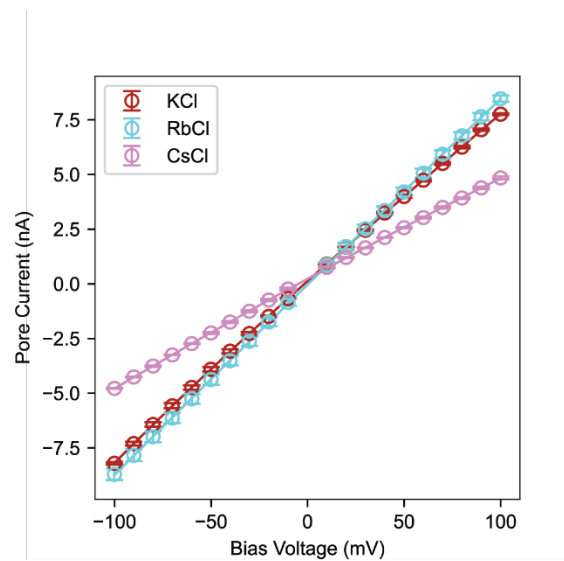
**Supplementary Fig. 9. KCl/MgCl<sub>2</sub> selectivity.** Data shown for all 20 devices tested with KCl and MgCl<sub>2</sub> salts, plotted against membrane resistance to KCl. Red circles are vertically aligned MoS<sub>2</sub> films, blue circles are horizontally aligned MoS<sub>2</sub> (also plotted in Fig. 3 a in the main text). The dotted red curve is a guideline. Test conditions are provided in Supplementary Table 1.

**a****b**

c

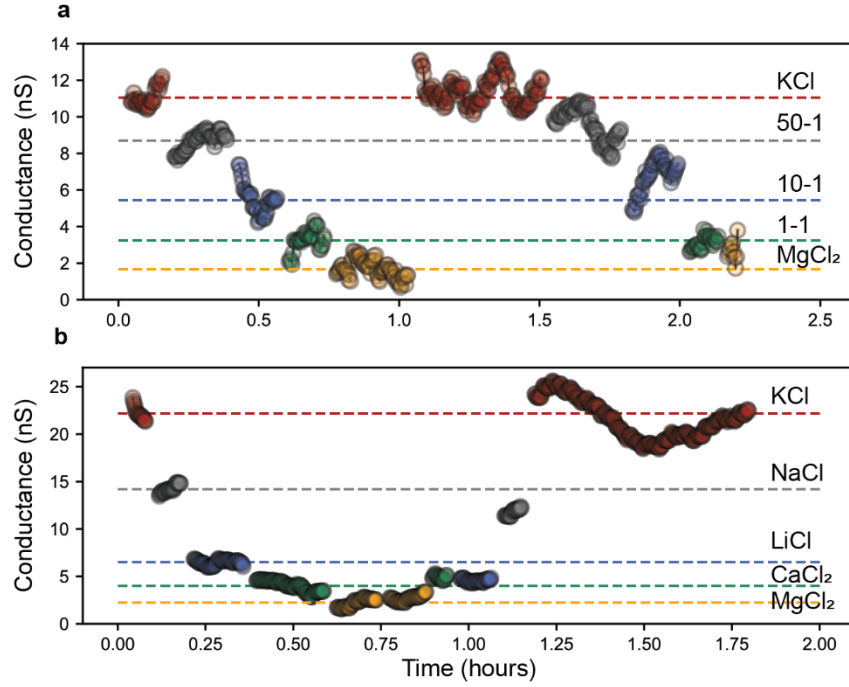


**Supplementary Fig. 10. I-V traces in 1 M salts.** Traces are shown for device 12 (a), device 7 (b) and device 8 (c), for which average selectivity data is shown in Fig. 3 of the main text. Each trace is an average of multiple ( $N \geq 3$ ) scans. Data is taken in increasing numerical order (KCl to MgCl<sub>2</sub> and MgCl<sub>2</sub> back to KCl).

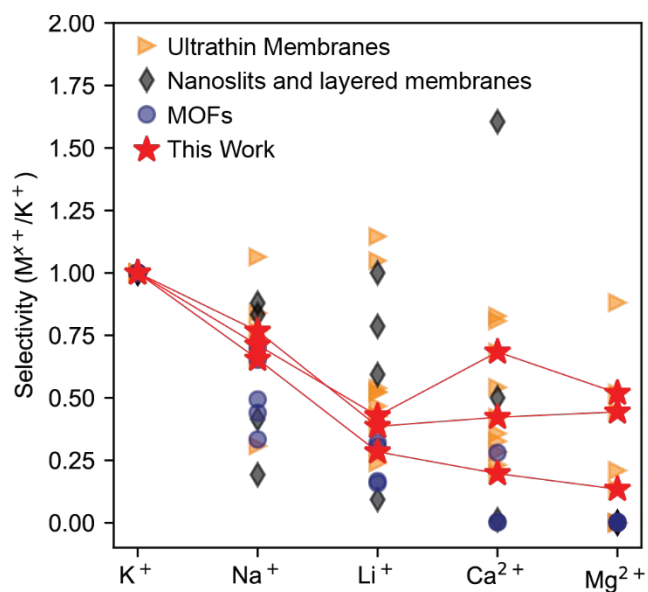


**Supplementary Fig. 11. I-V traces for CsCl and RbCl salts.** Curves shown for 1 M KCl, CsCl and RbCl through nanoporous CVD-MoS<sub>2</sub>. Test conditions are documented in Supplementary Table 2.

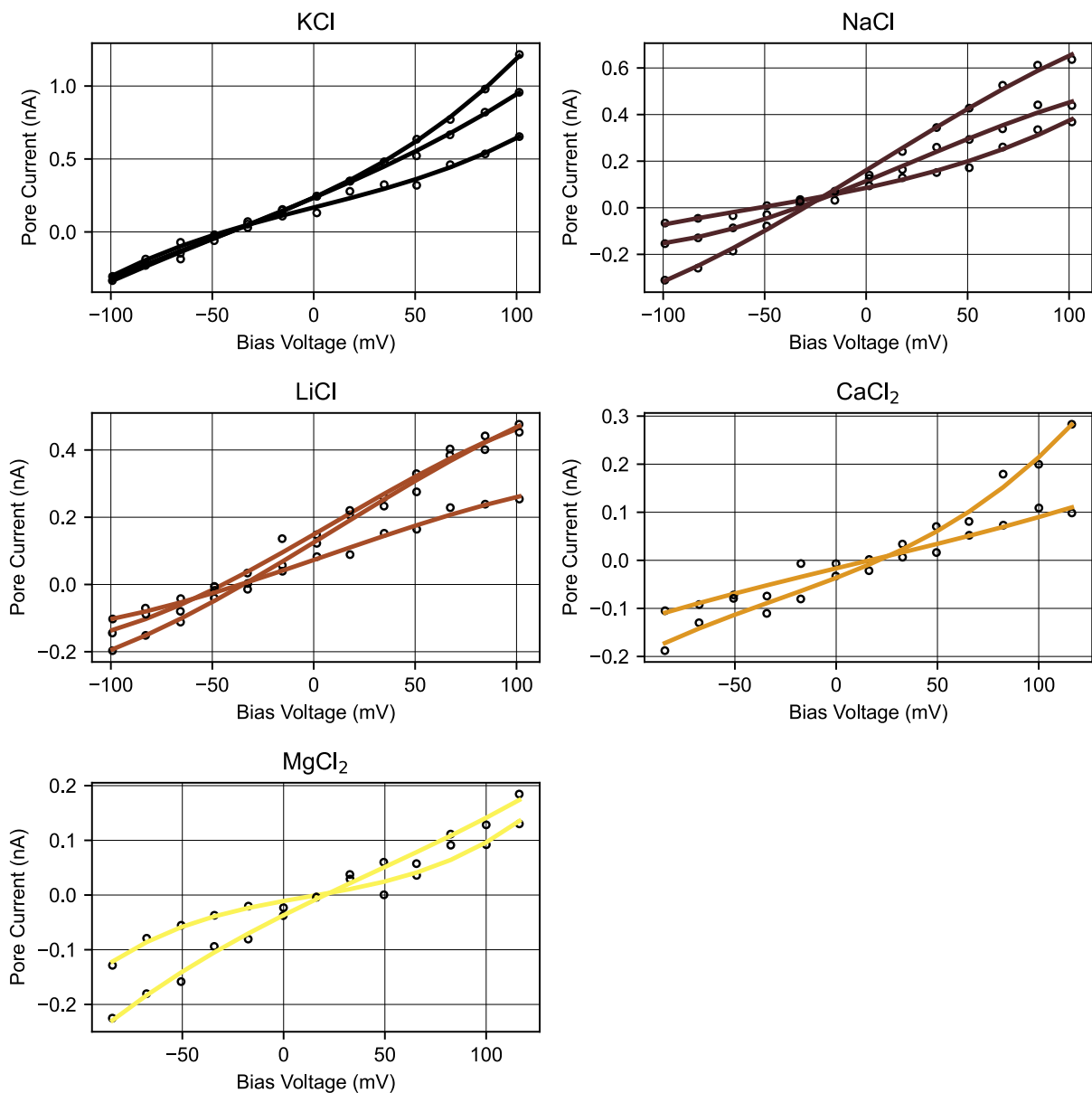




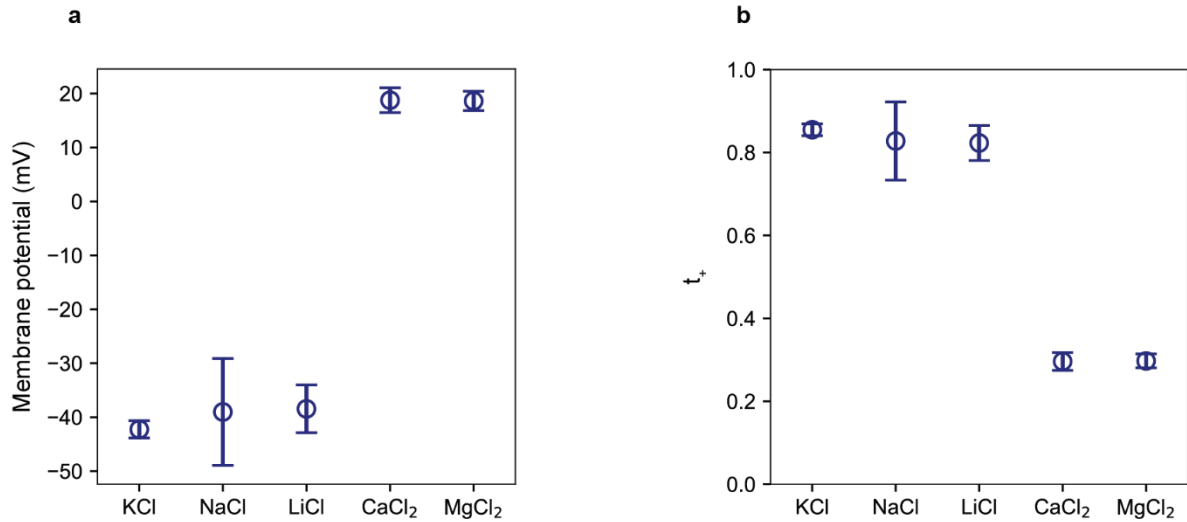
**Supplementary Fig. 12. Time series for electrolyte cycling.** Data shown over hour timescales, demonstrating pore stability. **(a)** Time series for cycling through electrolyte mixtures with different KCl/MgCl<sub>2</sub> molar ratios, corresponding to the data shown in Fig. 3 f, in the main text. **(b)** Time series for cycling through electrolyte mixtures for device 8 in Fig. 3, the device with the highest ion selectivity. Dotted lines represent average values for the first cycle.



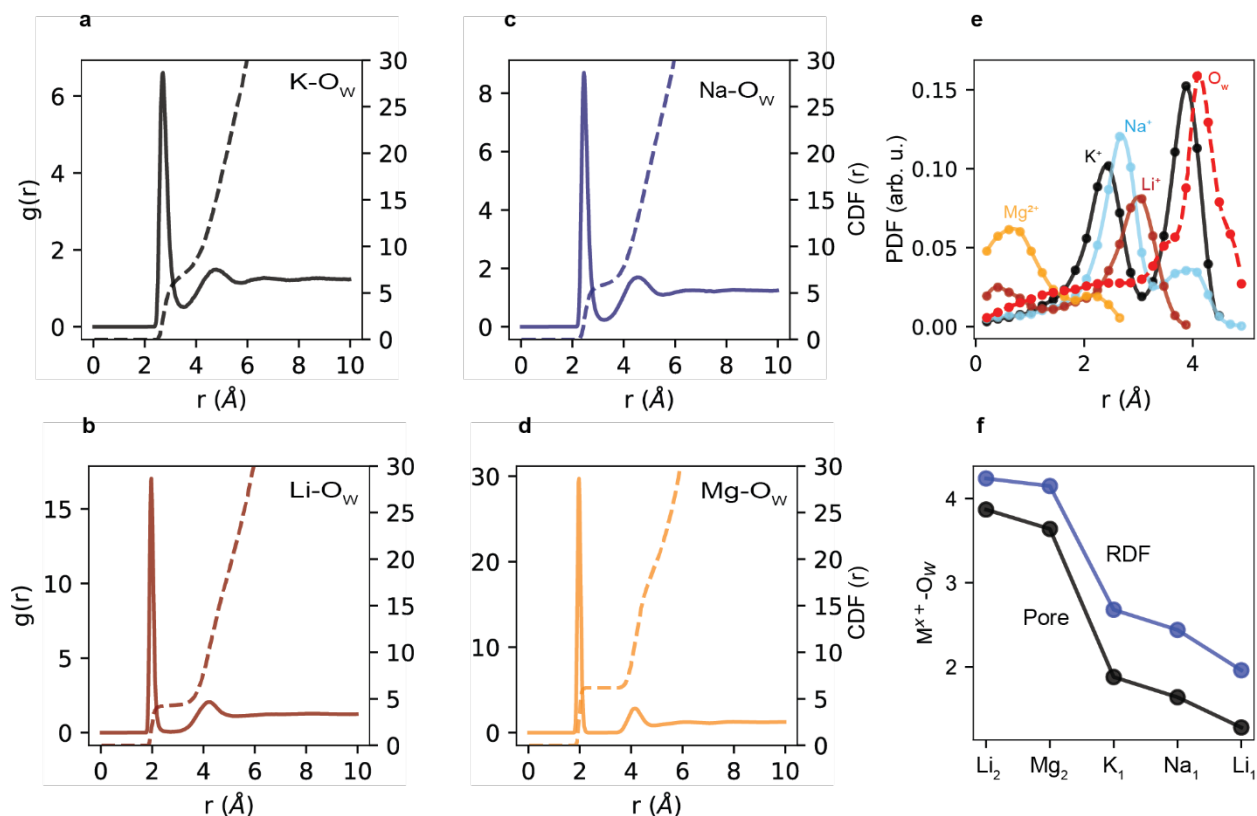
**Supplementary Fig. 13. Ion selectivity metrics in literature.** Comparison of selectivity data from this work and existing experiments with MOFs, solid-state nanopores and nanoslits. A comparison between this work and ultrathin membranes is in Fig. 3 of the main text. See Supplementary Table 3 for references and experiment details.



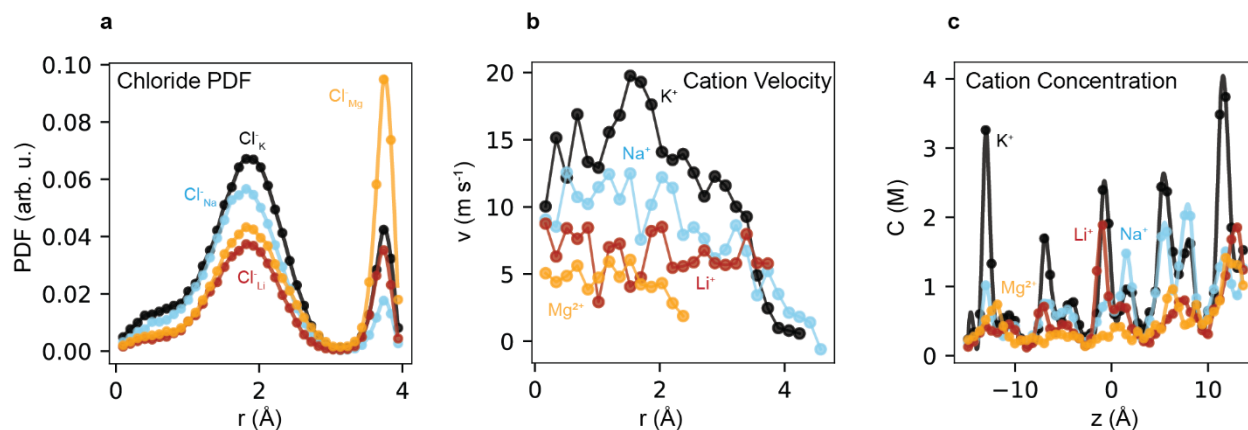
**Supplementary Fig. 14. Asymmetric electrolyte tests for transference number calculation.** Current-voltage curves with an asymmetric electrolyte (1M/0.1M) in the two reservoirs. The Nernst potential has been subtracted, so the membrane potential is found by measuring the x-intercept. Note the instability in the conductance is likely due to partial pore fouling during repeated testing and cycling through different salts.



**Supplementary Fig. 15. Membrane potential and transference number for various salts.** (a) Membrane potential for salts tested in 1M/0.1 M reservoirs (after the electrode potential is subtracted), from Supplementary Fig. 14. We note the qualitative difference for divalent salts compared to the monovalent salts tested in this study. (b) Transference numbers in a single membrane calculated from (a) showing relatively stable values for monovalent but a precipitous drop-off for divalent cations. The transference number is  $\sim 0.8$  for monovalent salts but is  $< 0.5$  for divalent salts, indicating the importance of both size exclusion and electrostatic effects in the pore. Error bars correspond to the standard error from the multiple ( $N \geq 2$ ) traces, shown in Supplementary Fig. 14.

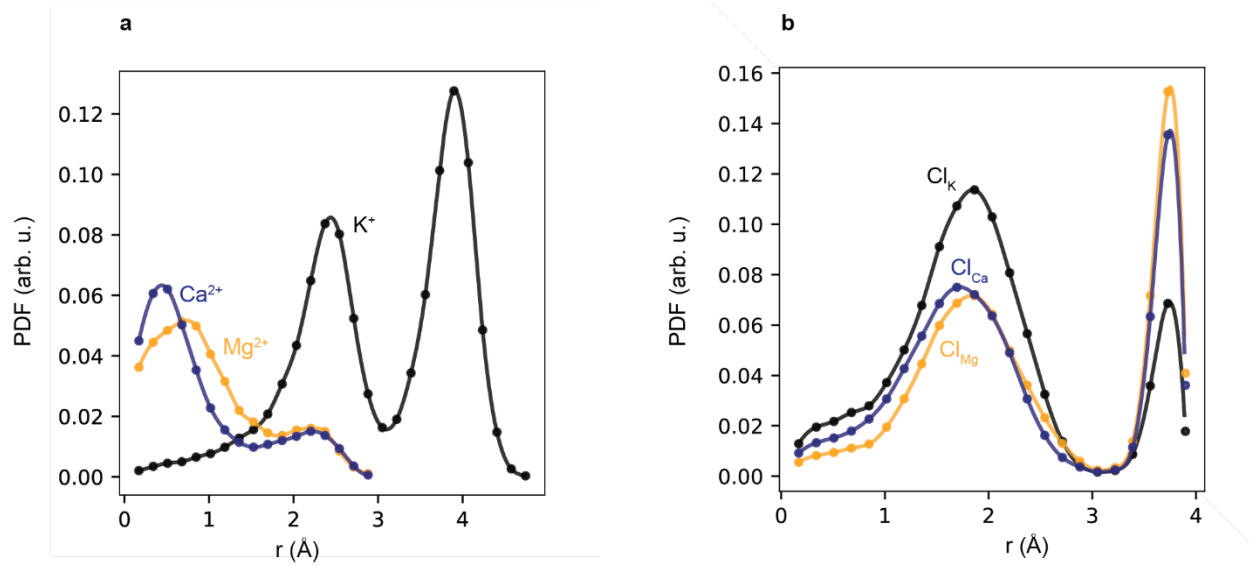


**Supplementary Fig. 16. Ion solvation structures calculated with molecular dynamics simulations. (a-d)** Cation-oxygen (M<sup>x+</sup>-O<sub>w</sub>) radial distribution functions,  $g(r)$ , (solid lines) and cumulative distribution functions,  $CDF(r)$ , (dashed line) for all simulated cations in the bulk reservoir. Radial distribution functions match existing literature, as do the coordination number in the 1<sup>st</sup> solvation shell for all cations<sup>3,4</sup>. **(e)** Probability density functions, as a function of radial coordinate within a 6L-1nm MoS<sub>2</sub> pore, normalized to K<sup>+</sup>, for all cations and oxygen. **(f)** Distance between the inner oxygen peak and the cation peaks (labelled from smallest to largest separation) in **e** compared to the corresponding peak in the RDF in **a-d**.

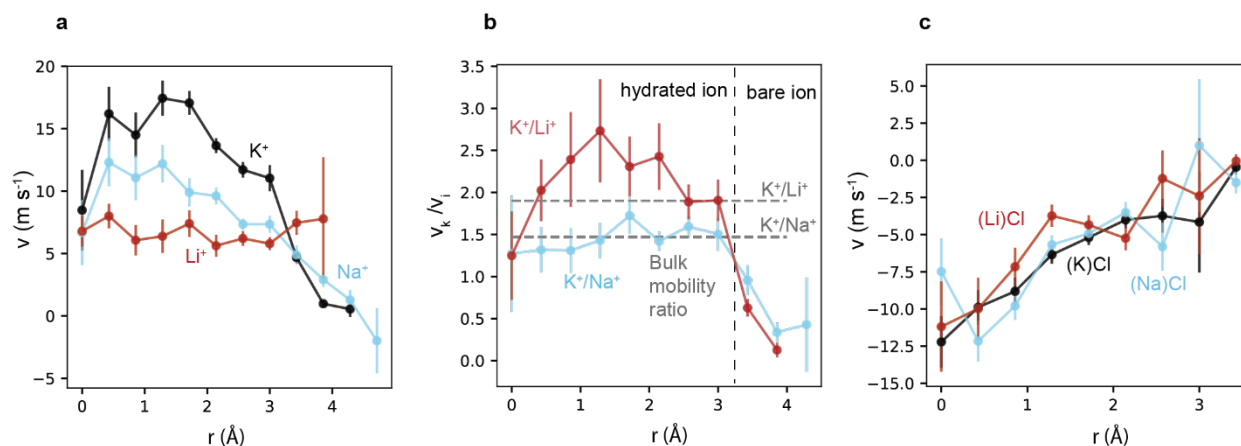


**Supplementary Fig. 17. Simulated anion concentration and cation velocity data.** (a) Anion concentration profiles for all simulated salts. The preferred positions of chloride ions are independent of the cation, although the relative preference for each position varies. (b) Velocity profiles for  $\text{K}^+$ ,  $\text{Na}^+$ ,  $\text{Li}^+$  and  $\text{Mg}^{2+}$  as a function of  $r$  for 6L-1nm MoS<sub>2</sub>. (c) Cation concentration as a function of the  $z$ -coordinate in the pore. Ions prefer to occupy the Van der Waals gap between layers, leading to the oscillating pattern seen here.

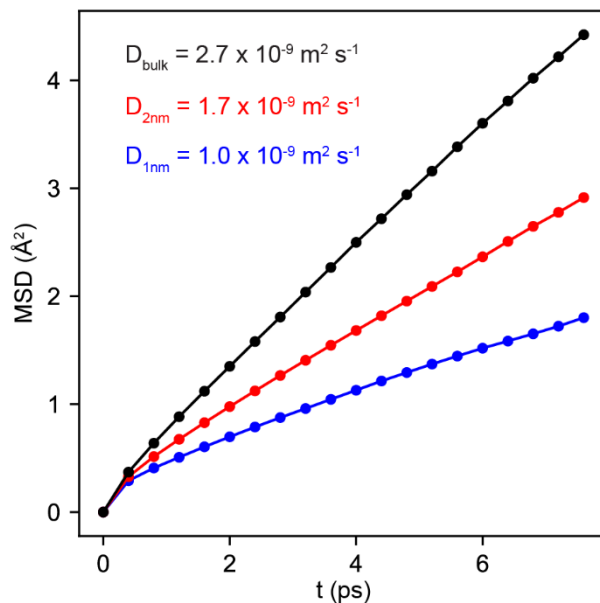




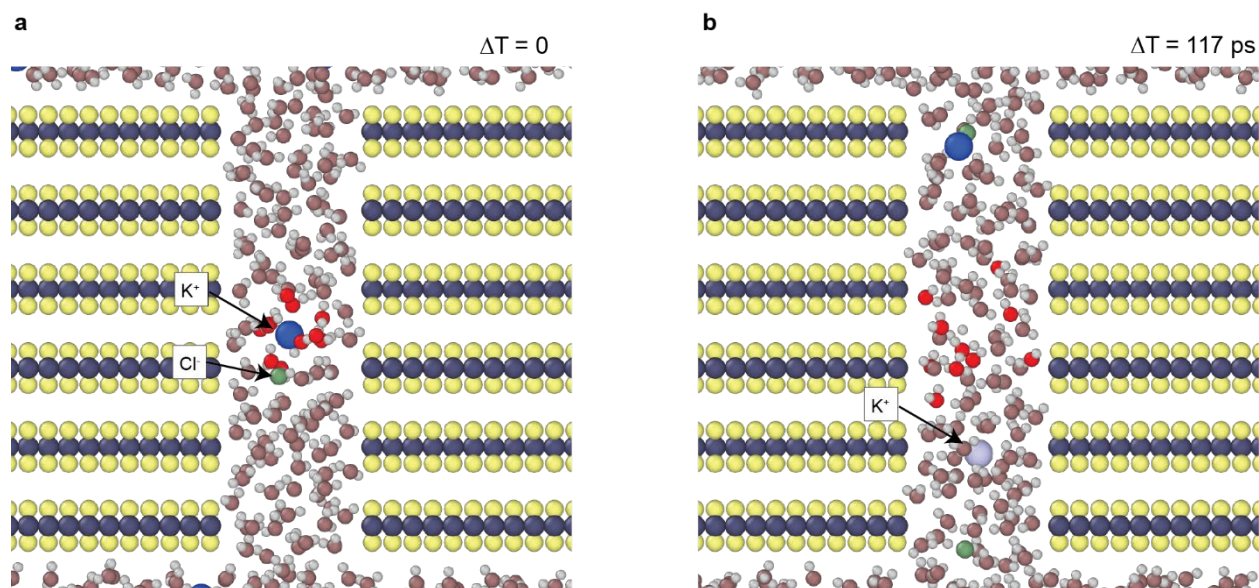
**Supplementary Fig. 18. Probability density functions for  $\text{CaCl}_2$ .** As in Fig. 4 g in the main text the data are normalized to  $\text{K}^{+}$ , for each ion inside the 6L-1nm pore. As in Fig. 4 g, three distinct regions are apparent, corresponding to different hydration levels.  $\text{Ca}^{2+}$  and  $\text{Mg}^{2+}$  show similar profiles, but differ dramatically from that of  $\text{K}^{+}$ , due to their much larger hydration energies.



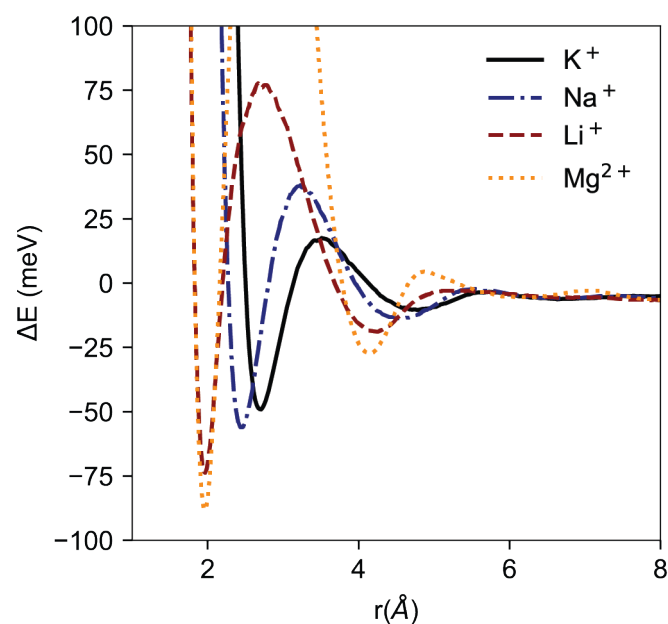
**Supplementary Fig. 19. Radial velocity profiles for monovalent ions.** (a) Simulated velocity profiles for the monovalent ions K<sup>+</sup>, Na<sup>+</sup>, and Li<sup>+</sup>. A decay in velocity is observed for K<sup>+</sup> and Na<sup>+</sup> as the ions approach the pore wall. Li<sup>+</sup> remains hydrated (does not directly contact the wall) so the velocity does not decay at the pore edge. Because the distribution of K<sup>+</sup> ions is shifted towards the center of the pore relative to Na<sup>+</sup> (Fig. 4 main text) their average speed is higher. (b) Ratio of velocities (and the ratio of bulk mobilities) for the monovalent ions. Excluding ions at the pore edge, K<sup>+</sup> is significantly faster, even relative to its bulk value, than Li<sup>+</sup>. (c) Radial velocity profiles for chloride in the different monovalent salts. The velocity profile does not depend on cation identity, indicating that the concentration of anions is the sole determinant of total anionic flux. Error bars correspond to the standard error measured over the entirety of the simulation trajectory (Supplementary Methods).



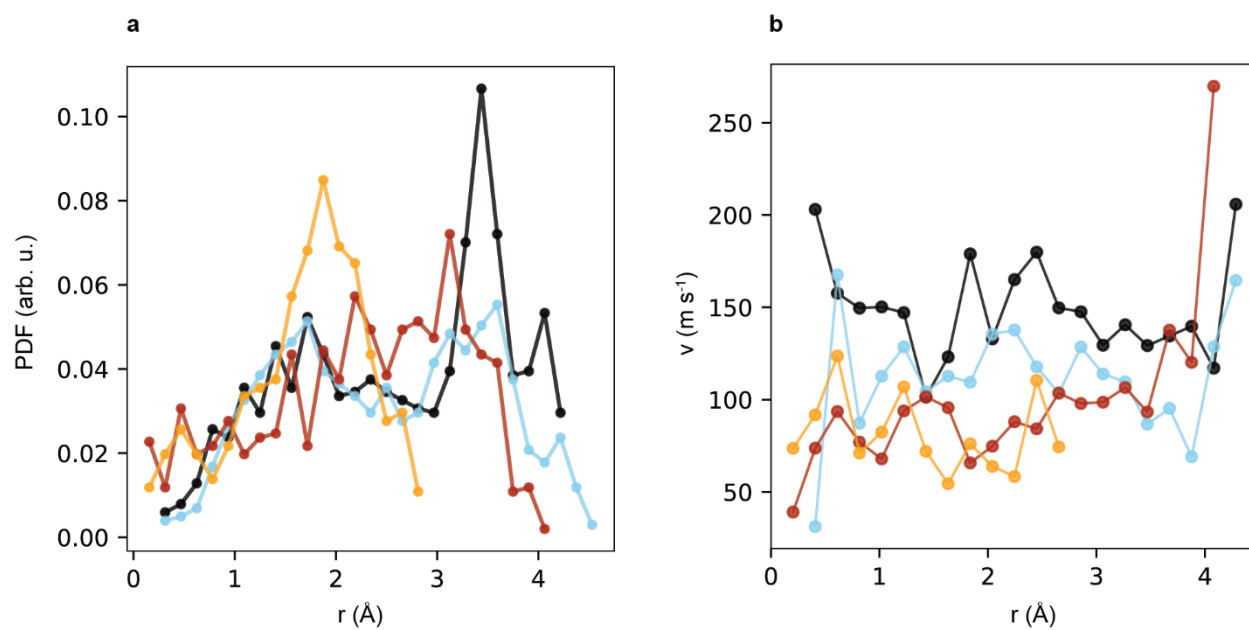
**Supplementary Fig. 20. Calculation of water diffusion coefficients.** Mean squared displacement (MSD) of water molecules in the reservoirs of the simulation box (bulk) and in a 6L-2nm (red) and 6L-1nm (blue) MoS<sub>2</sub>. These data are calculated during a separate simulation run, in which no bias is applied across the simulation box and cations are added only to neutralize the MoS<sub>2</sub> surface charge. The bulk self-diffusion coefficient calculated from the MSD, which is in good agreement with the existing literature<sup>5</sup>, is nearly three times as large for the bulk value compared to water confined to the 1 nm pore.



**Supplementary Fig. 21. Molecular dynamics snapshots showing water transport relative to ion motion.** Molecular dynamics snapshots of ions (blue and green spheres) and water (red and gray spheres) in MoS<sub>2</sub> nanopores, with (a) 117 ps before (b). In both snapshots, the same water molecules and K<sup>+</sup> ion are highlighted in bright red and blue, respectively. As the K<sup>+</sup> ion traverses the pore, it constantly exchanges its hydration shell, which remains mostly stuck in place.

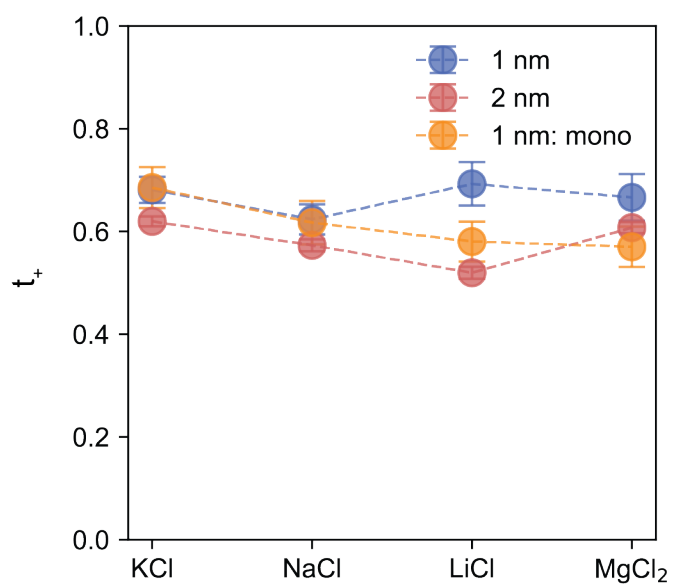


**Supplementary Fig. 22. Radial energy profiles for  $M^{x+}$ - $O_w$  interactions.** These data are calculated via a Boltzmann-inversion of radial distribution functions (Supplementary Fig. 16).  $Li^+$  and  $Mg^{2+}$  show distinctly stronger interactions with the inner hydration shell, relative to  $K^+$  especially, but also  $Na^+$ . Stronger interactions with the solvating water molecules lead to a reduced exchange rate and, therefore, slower ion migration.

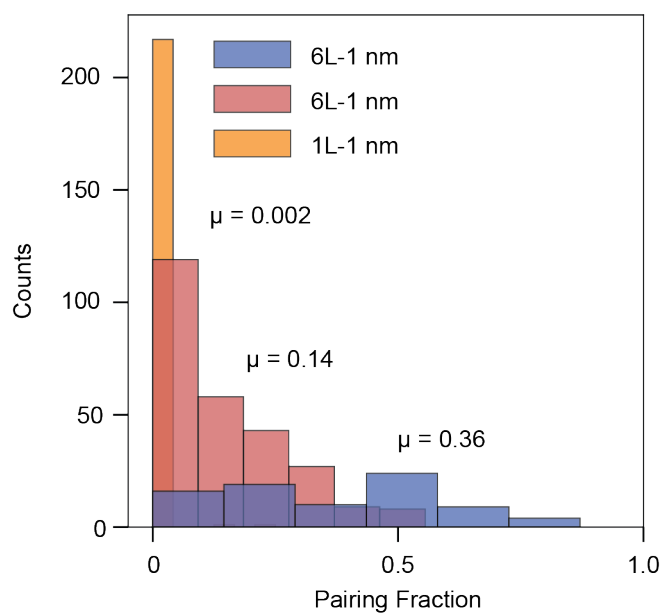


**Supplementary Fig. 23.** Monolayer PDFs. Radial probability density function (a) and velocity profile (b) for ions in a 1 nm monolayer pore.

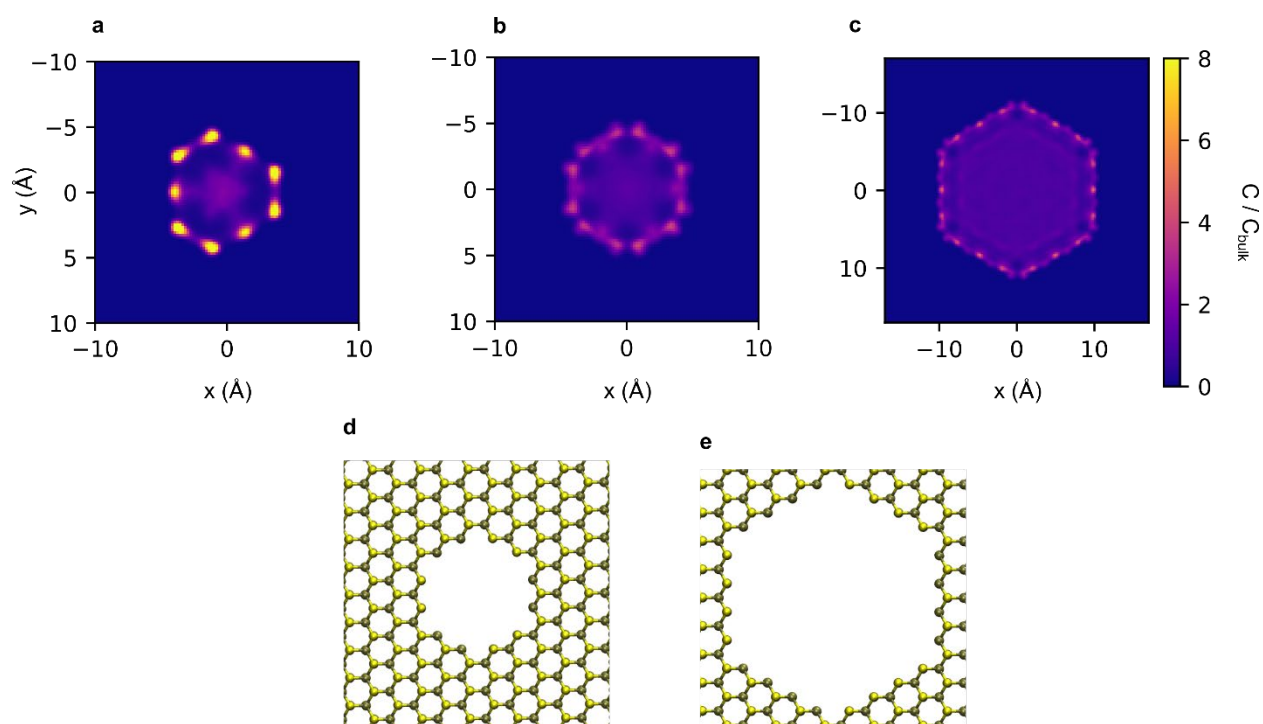




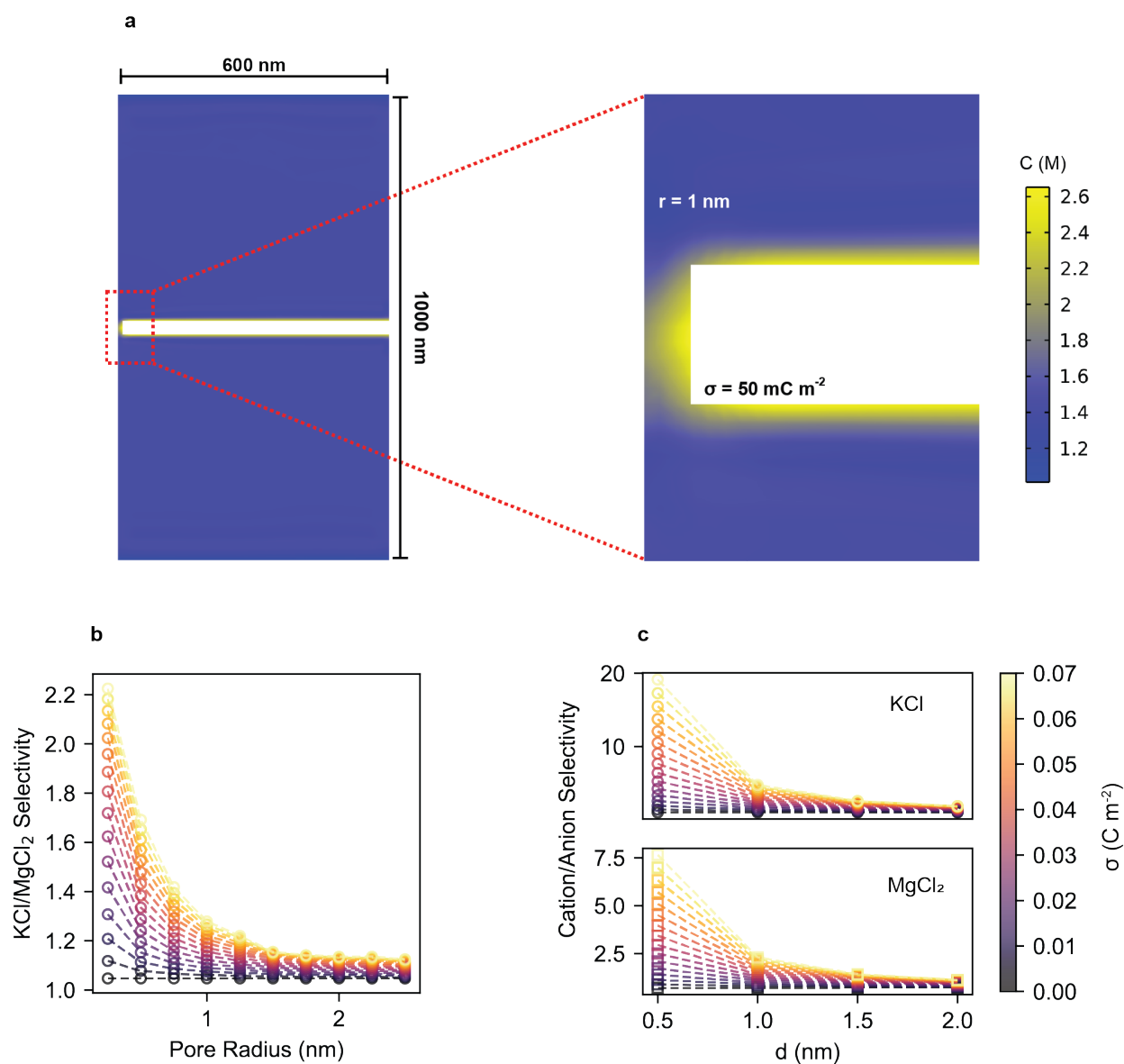
**Supplementary Fig. 24.** Simulated transference numbers. Transference number for various salts, calculated using the values in Supplementary Table 4. Error bars correspond to the standard error measured over the entirety of the simulation trajectory (Supplementary Methods).



**Supplementary Fig. 25. Ion pairing in nanopores.** The number of cations that are paired ( $d < l_B$ ) with an anion for a given fraction of the duration it takes for the cation to pass through the pore. Mean pairing fraction is given, showing that the ions are effectively non-interacting in the monolayer but are strongly coupled in the six-layer film.



**Supplementary Fig. 26. Oxygen (water) density profiles.** Data shown for a (a) 1 nm diameter pore in monolayer, a (b) six-layer  $\text{MoS}_2$  film and a (c) 2 nm diameter pore in a six-layer  $\text{MoS}_2$  film. **d-e**, Crystal structure of a 1 nm and 2 nm diameter pore in a  $\text{MoS}_2$  film, oriented to match the water density profiles in a-c.



**Supplementary Fig. 27. Finite element simulations results.** (a) Geometry of finite element simulations, with the steady-state concentration of  $\text{K}^+$  given by the color distribution. The pore size and surface charge is tuned across a range of values; here,  $r = 1 \text{ nm}$  and  $\sigma = 50 \text{ mC m}^{-2}$ . (b) Salt selectivity as a function of pore radius and surface charge, with the color bar given in (c). (c) Cation-anion selectivity as a function of pore diameter and surface charge.

## Supplementary Tables

Sample	G <sub>KCl</sub> (nS)	G <sub>MgCl<sub>2</sub></sub> (nS)	Pulse Voltage (V)	Pulse Time (ms)	Pulse Number	Mo Seed Thickness (nm)
1	2.0	0.1	1.5	5	1	1.75
2	5.4	0.6	1.5	5	1	1.75
3	7.9	1.9	1.5	5	1	1.75
4	9.4	2.7	0.4-0.5	NA	NA	1.75
5	10.8	1.0	1.5	5	1	1.75
6	11.8	1.9	0.4-0.5	NA	NA	1.75
7	21.8	9.7	1.5	10	2	1.75
8	23.4	3.2	1.5	10	1	1.75
9	24.6	10.0	1.5	5	1	1.75
10	27.6	11.0	1.5	25	1	2.0
11	31.4	18.2	1.5	10	1	2.0
12	37.1	19.2	1.5	10	2	1.75
13	48.3	16.9	1.5	5	1	1.75
14	228.5	197.6	1.5	50	2	2.0
15	234.0	114.0	0.4-0.5	NA	NA	1.75
16*	18.8	5.6	0.4-0.5	NA	NA	15.0
17	27.0	4.6	1.5	5	4	15.0
18*	42.0	12.6	0.4-0.5	NA	NA	15.0
19*	51.1	28.0	0.4-0.5	NA	NA	15.0
20*	91.0	88.0	0.4-0.5	NA	NA	10.0

**Supplementary Table 1. Devices tested for KCl/MgCl<sub>2</sub> selectivity.** Test conditions and results for 20 different devices, used to measure the selectivity of KCl and MgCl<sub>2</sub>. Samples were collected over the course of one year. Different film thickness and pulse frequencies were used, although in the ranges tested here there was little effect on the results. The concentration of salts is 1 M, except for those rows marked with a \*, which were measured with 0.1 M salts. Current-voltage curves for these data are shown in Supplementary Fig. 8.

	Ion conductance (nS)							Pore generation conditions		
	G <sub>KCl</sub>	G <sub>NaCl</sub>	G <sub>LiCl</sub>	G <sub>CaCl<sub>2</sub></sub>	G <sub>MgCl<sub>2</sub></sub>	G <sub>CsCl</sub>	G <sub>RbCl</sub>	Pulse Voltage (V)	Pulse Time (ms)	Pulse Number
Device 8	23.4 (1.0)	15.3 (1.0)	6.6 (0.6)	4.6 (0.3)	3.15 (0.2)	-	-	1.5	10	1
Device 7	21.8 (2.0)	16.7 (1.6)	8.42 (0.9)	9.21 (0.9)	9.68 (0.7)	-	-	1.5	10	2
Device 12	37.1 (2.6)	26.4 (1.0)	15.8 (1.5)	25.3 (1.0)	19.23 (0.7)	-	-	1.5	10	2
-	80.0 (3.0)	-	-	-	-	48.0 (2.0)	86.0 (1.0)	2	10	2

**Supplementary Table 2.** Three horizontally aligned MoS<sub>2</sub> devices, of the 20 total devices tested for both divalent *and* monovalent salt selectivity. Another device is tested with KCl, CsCl and RbCl salts. Test conditions and results for these different devices, used to measure the selectivity of KCl, NaCl, LiCl, CaCl<sub>2</sub> and MgCl<sub>2</sub>; or KCl, CsCl and RbCl. Standard errors for a given element in the table are included in parentheses. All Mo seed film thicknesses were 1.75 nm, and the salt concentration is 1 M. Current-voltage curves for these data are shown in Supplementary Fig. 10 and Supplementary Fig. 11.



KCl	NaCl	LiCl	CaCl <sub>2</sub>	MgCl <sub>2</sub>	Unit	Concentration for test (M)	Thick (nm)	Type	Ref
0.25	0.11		0.07	0.03	mol m <sup>-2</sup> h <sup>-1</sup>	0.5	1000	MOF	Liu et al. 2023 <sup>6</sup>
4.74	3.09	1.52	0.007	0.002	nS	0.1	12000	MOF	Lu et al., 2020 <sup>7</sup>
1.07	0.53	0.17		0.000	mol m <sup>-2</sup> h <sup>-1</sup>	0.1	600	MOF	Xu et al. , 2020 <sup>8</sup>
1.77	0.59	0.54			mol m <sup>-2</sup> h <sup>-1</sup>	5.00E-03	600	MOF	Gao et al. 2019 <sup>9</sup>
0.3	0.21	0.05	0.0009	0.0008	nS	0.1	12000	MOF	Lu et al., 2021 <sup>10</sup>
0.006	0.005	0.006	7.00E-05	3.00E-06	mol m <sup>-2</sup> h <sup>-1</sup>	1	1.00E+05	Graphene oxide	Abraham et al. 2017 <sup>11</sup>
1.18	0.85	0.7	0.59	0.47	S m <sup>-1</sup>	0.1	7000	2D Angstrom slits	Esfandiar et al. 2017 <sup>12</sup>
0.021	0.019	0.017	0.034	0.034	S m <sup>-1</sup>	0.1	3000	Dyed MoS <sub>2</sub>	Hirunpinyopas et al. 2019 <sup>13</sup>
0.183	0.076	0.017		0.005	mol m <sup>-2</sup> h <sup>-1</sup>	0.1	2160	Graphene Oxide	Xi et al. 2018 <sup>14</sup>
0.026	0.005			0.000	mol m <sup>-2</sup> h <sup>-1</sup>	0.1	1500	Graphene Oxide	Song et al. 2018 <sup>15</sup>
5.67	4.76	2.41	3.07	2.73	nS	0.1	0.3	Graphene nanopores	Fu et al. 2020 <sup>16</sup>
2.3		1.2	0.75	0.41	nS	0.1	0.3	Graphene nanopores	Jain et al. 2015 <sup>17</sup>
2.6		1.4	2.1	0.8	nS	0.1	0.3	Graphene nanopores	Jain et al. 2015 <sup>17</sup>
4.2		2.2	1.5	1.3	nS	0.1	0.3	Graphene nanopores	Jain et al. 2015 <sup>17</sup>
0.85	5	4	5	2.3	nS	1	0.6	MoS <sub>2</sub> nanopores	Feng et al. 2016 <sup>18</sup>
0.76		0.86		0.66	nS	1	0.6	MoS <sub>2</sub> nanopores	Priyanka et al. 2020 <sup>19</sup>
17.1	11.3	8.0	4.8	3.6	nS	1	0.3	Graphene nanopores	Rollings et al. 2016 <sup>20</sup>
0.58	0.18	0.14	0.13	0.1	nS	0.1	0.3	Graphene/PET	Su et al. 2022 <sup>21</sup>
0.0024	0.0026	0.0025	0.0020		mol m <sup>-2</sup> h <sup>-1</sup>	1.00E-04	0.3	Graphene nanopores	Wyss et al. 2019 <sup>22</sup>
23.4 (1.0)	15.3 (1.0)	6.6 (0.6)	4.6 (0.3)	3.15 (0.2)	nS	1	8	MoS <sub>2</sub> nanopores	This work
21.8 (2.0)	16.7 (1.6)	8.42 (0.9)	9.21 (0.9)	9.68 (0.7)	nS	1	8	MoS <sub>2</sub> nanopores	This work
37.1 (2.6)	26.4 (1.0)	15.8 (1.5)	25.3 (1.0)	19.23 (0.7)	nS	1	8	MoS <sub>2</sub> nanopores	This work

**Supplementary Table 3. Ion selectivity metrics in literature.** References and selectivity mechanism for the data depicted in Supplementary Fig. 13. When raw data is unavailable, we extract values using an online figure digitizer. A few notes on specific experiments is as follows. First, certain values of conductance had to be extracted directly from I-V curves; here, we used the average at the minimum and maximum voltages. In order to calculate the conductance for Feng *et al.*<sup>18</sup>, which varies significantly with voltage, we take the value at 0 V. For Rollings *et al.*<sup>20</sup>, we use data in their Fig. 3 c, as opposed to that in their Fig. 3 b. We do so because the pore size in Fig. 3 c is well-defined and ~2 nm (as opposed to Fig. 3 b, where the pore size is, according to conductance values, significantly larger). Furthermore, Fig. 3 c displays typical selectivity vs conductance trends, which are not followed in Fig. 3 b. For Jain *et al.*<sup>17</sup>, we note that the concentration of divalent salts is 0.5 M. When reporting thickness, tortuosity is not accounted for. When selectivity is measured in 0.1 M salts, we estimate the 1 M conductance displayed in Fig. 3 by scaling by a factor of 10.

Total				Cation						Anion					
Pore		Current		Current (nA)		Velocity (m s <sup>-1</sup> )		Concentration (M)		Current (nA)		Velocity (m s <sup>-1</sup> )		Concentration (M)	
6L-1 nm	KCl	0.96	0.02	0.65	0.02	8.01	0.17	1.079	0.003	0.31	0.02	-5.03	0.22	0.804	0.003
	NaCl	0.67	0.01	0.42	0.01	7.36	0.22	0.753	0.002	0.25	0.01	-5.67	0.28	0.590	0.002
	LiCl	0.39	0.01	0.27	0.01	6.56	0.28	0.551	0.002	0.12	0.01	-3.76	0.32	0.427	0.002
	MgCl <sub>2</sub>	0.50	0.02	0.34	0.02	4.44	0.23	0.499	0.002	0.17	0.01	-3.23	0.22	0.686	0.002
	CaCl <sub>2</sub>	0.43	0.02	0.25	0.02	3.74	0.21	0.44	0.002	0.18	0.01	-3.5	0.20	0.686	0.002
6L-2 nm	KCl	8.73	0.06	5.41	0.07	22.46	0.13	0.552	0.001	3.32	0.05	-20.35	0.19	0.374	0.001
	NaCl	6.37	0.06	3.65	0.06	16.66	0.13	0.502	0.001	2.72	0.05	-16.88	0.19	0.369	0.001
	LiCl	5.50	0.05	2.86	0.05	15.08	0.14	0.434	0.001	2.64	0.05	-18.58	0.21	0.326	0.001
	MgCl <sub>2</sub>	8.11	0.07	4.93	0.07	17.66	0.15	0.320	0.001	3.19	0.06	-14.34	0.13	0.509	0.001
1L-1 nm	KCl	3.65	0.09	2.50	0.11	141.4	4.2	0.233	0.008	1.15	0.08	-225.64	8.59	0.067	0.004
	NaCl	2.80	0.09	1.73	0.09	113.2	4.4	0.201	0.007	1.07	0.08	-225.22	10.03	0.063	0.004
	LiCl	2.52	0.08	1.46	0.07	89.20	3.33	0.216	0.007	1.06	0.08	-176.15	8.91	0.079	0.004
	MgCl <sub>2</sub>	3.36	0.10	1.92	0.11	76.26	2.96	0.166	0.006	1.45	0.09	-200.83	7.48	0.095	0.005

**Supplementary Table 4. Simulated ion transport metrics.** Current, average velocity and average concentration of ions inside various pores. The first column in a given section is the measured value, and the second column is the standard error, estimated by calculating the variation in a given output over the course of the simulation. We note that although average velocities for ions differ significantly, the values match expectation give bulk mobilities.

Element	$\epsilon_i$ (kcal mol <sup>-1</sup> )	$\sigma_i$ (Å)	Charge (e)
H <sup>23</sup>	0.00	0.00	0.3
O <sup>23</sup>	0.155	3.16	-0.6
K <sup>24</sup>	0.583	2.69	1
Na <sup>24</sup>	0.100	2.58	1
Li <sup>25,26</sup>	0.167	2.95	1
Mg <sup>27</sup>	0.140	1.63	2
Ca <sup>27</sup>	0.224	2.41	1
Cl <sup>24,27</sup>	0.100	4.40	-1
Mo <sup>28</sup>	0.130	2.55	-0.76
S <sup>28</sup>	0.250	3.50	0.38

**Supplementary Table 5.** Lennard-Jones parameters and partial charges used for MD simulations.

## Supplementary Notes

### Finite Element Simulations of Ion Transport

Finite element (FE) simulations based on the standard Poisson-Nernst-Planck (PNP) model ignore both ion correlations and finite-size effects<sup>29</sup>. For salts with similar bulk conductivities, such as for  $\text{MgCl}_2$  and  $\text{KCl}$ , FE simulations effectively isolate the electrostatic interactions between the ions and the channel wall. We focus on this pair because the effect of ion valence dominates in the absence of size effects. Due to the relatively small computational complexity of FE simulations, we are able to simulate a large fraction of the parameter space, varying both surface charge and pore diameter.

The Poisson-Nernst-Planck equations, detailed elsewhere<sup>29</sup>, are solved in COMSOL Multiphysics version 6.0.0.354 with the Transport of Diluted Species and Electrostatics modules. We assume the pore is cylindrical and thereby enforce an axisymmetric symmetry and solve the PNP equations in two-dimensional ( $r, z$ ) space. We use an adaptive triangular mesh. The geometry is schematized in Supplementary Fig. 27 a. We parameterize the model with the surface charge and pore diameter, allowing the former to vary from 0-0.075  $\text{C m}^{-2}$  and the latter to vary from 0.5-5 nm. The concentration of cations is set at 1 M, and a 1V bias is applied across the pore.

Even in 1 M electrolytes, where the Debye length is  $\sim 0.3$  nm, significant deviations from bulk behavior are observed for moderate to high surface charge densities. First, we measure the  $\text{KCl}/\text{MgCl}_2$  selectivity for pores with a diameter of 0.5 to 5 nm (Supplementary Fig. 27 b). The largest pores fail to discern  $\text{KCl}$  and  $\text{MgCl}_2$ .  $\text{KCl}$  has a significantly higher conductance than  $\text{MgCl}_2$  through pores  $< 2$  nm with a surface charge  $> .025 \text{ C m}^{-2}$ . As the chloride contribution is a small fraction of the total current for these pores (Supplementary Fig. 27 c), we attribute this difference to the cation alone. For a small enough pore with a large enough surface charge, the number of charge carriers will increase to neutralize the pore.  $\text{Mg}^{2+}$  is multivalent, so fewer ions are required to neutralize the pore, concentration in, and therefore the current through, the pore. We note that the selectivity measured via FE simulations is smaller than that measured in MD simulations under similar conditions, as the FE simulations only account for electrostatic effects.

## Supplementary Methods

### Molecular Dynamics Simulations

We build 2H-phase  $\text{MoS}_2$  slabs with one or six layers that separate two 1 M electrolyte reservoirs. Mo and S atoms are deleted within a given radius in the center of the slab to create a pore. Each reservoir is 7.5 nm in height, and 3 nm in width and depth. The simulation is periodic in all three dimensions. Lennard Jones (LJ) parameters are tabulated in Supplementary Table 5 and cross-terms are calculated using the Lorentz-Berthelot mixing rules<sup>30</sup>. The mixing rule for  $\text{MgCl}_2$  is modified to increase the interaction strength between Mg and Cl, as determined by Mamatkulov *et al.*<sup>27</sup> To retain consistency between ions, we use parameters that are optimized with the same set of simulation conditions (the same parameters for both anion and water). Water is modelled explicitly using the SPC/E model, and the bonds are held rigid using the SHAKE algorithm<sup>31</sup>. The atoms in the  $\text{MoS}_2$  sheet are fixed. Likely due to hydroxyl adsorption, wetted pores in  $\text{MoS}_2$  are negatively charged<sup>32</sup>. We model this effect by adding an additional charge to all Mo and S atoms exposed to the electrolyte, such that the total surface charge density is  $-50 \text{ mC m}^{-2}$ . To obtain an accurate picture of water dynamics inside the pore, we perform an

additional set of simulations with the same parameters, excluding both an applied electric field and the salt. Additional cations are, however, added to compensate for the negative surface charge of the MoS<sub>2</sub> film.

Molecular dynamic simulations were performed using the LAMMPS package<sup>33</sup>. The initial configuration is calculated using Packmol<sup>34</sup> and the water bonds set by TopoTools in Visual Molecular Dynamics<sup>35</sup>. First, we run an NPT ensemble for 0.5 ns, at which time the pore is entirely filled with water molecules and all thermodynamic variables have stabilized. Then we carry out a production run with an NVT ensemble for 8-20 ns. The pure-water simulations are run for 0.5 ns. Analysis is carried out using MDAnalysis<sup>36</sup> software in Python. Ionic current is calculated by extracting average drift velocity of ions (motion parallel to the electric field),  $v_z$  and number density  $n$  through  $J = qnv_z$ , where  $q$  is the ion charge and  $J$  the current. Average velocity is calculated by averaging the gradient of position in the  $z$  direction over all ions in the pore through the course of the simulation. All code and simulation scripts are available on request.

### Calculation of Transference Number via Ion Transport Measurements

To determine the transference number for a given salt solution, we measure the current voltage trace (Supplementary Fig. 14) and extract the zero-current voltage. We account for electrode potential difference, given by the Nernst equation:

$$V_n = \ln \Delta \frac{RT}{nF}, \quad (1)$$

where  $\Delta$  is the concentration ratio between the two sides of the reservoir, and  $n$  is unity (the number of electrons exchanged in the silver chlorination/de-chlorination half-reactions). The membrane voltage is then  $V_m = V_0 - V_n$ . The mobility ratio is determined through the Henderson equation<sup>12,37</sup>:

$$\frac{\mu_+}{\mu_-} = - \frac{z_+ \ln \Delta - z_- FV_m / RT}{z_- \ln \Delta - z_+ FV_m / RT} \quad (2)$$

Using the relation  $J_i = z_i c_i \mu_i E$  and noting that the product  $z_i c_i$  as well as  $E$  are equal for cation and anions for both mono and divalent salts, the transference number is simply:

$$t_+ = \frac{1}{1 + \frac{\mu_-}{\mu_+}} \quad (3)$$

### Calculation of Pore Size Distributions and Expected Conductance

In the following, we make phenomenological arguments to approximate the conductance of heterogeneous porous array. To estimate conductance of a close-packed, heterogeneous distribution of pores, we modify two models, one of which incorporates the effect of surface charge and the other of access-resistance in a two-dimensional pore array. The conductance of an uncharged, isolated pore with  $\frac{d}{L} \ll 1$  (where  $d$  is the pore diameter and  $L$  the pore length) is proportional to the bulk conductance of the electrolyte  $k_b$ , and the ratio of pore area to pore length. When  $\frac{d}{L} \sim 1$ , however, we must account for access resistance: following Gadaleta *et al.*<sup>38</sup>, we add an additional term in series with the pore resistance:

$$G = k_b \left( \frac{4L}{\pi d^2} + \frac{1}{d} \right)^{-1} \quad (4)$$

Eq. 4 neither accounts for pore-pore interactions nor surface charge, theories for both of which have been well studied. Choongyeop *et al.*<sup>39</sup> derive a relationship between conductance and surface charge that describes the common conductance plateau at low concentrations, wherein the conductance at low concentration is determined by the surface charge and pore geometry, rather than charge carrier number in the bulk:

$$G = k_b \left( \frac{4L}{\pi d^2} \frac{1}{1 + 4 \frac{l_{Du}}{d}} + \frac{2}{\alpha d + \beta l_{Du}} \right)^{-1} \quad (5)$$

Where  $l_{Du}$  is the so-called Dukhin length, which is the ratio of surface to bulk conductivities, and scales linearly with surface charge and inversely with bulk concentration.  $\alpha$  and  $\beta$  are geometrical factors and can be approximated to be two here<sup>32,39</sup>. Gadaleta *et al* derive a scaling relationship for the conductance of close-packed 2D array of homogeneous pores that effectively increases the access resistance of any given pore in the array by introducing an effective diameter  $d_{eff}$ :

$$G = k_b \left( \frac{4L}{\pi d^2} + \frac{1}{d_{eff}} \right)^{-1}$$

$$d_{eff} \approx \frac{d}{1 + \gamma_N \frac{d}{2L}} \quad (6)$$

where  $\gamma_N \approx \sqrt{N}$  for large  $N$ . Here, we note that Gadaleta *et al* derive the scaling relationship for  $\gamma_N$  by noting that, for large  $N$ , the capacitance (and thus the effective diameter of the pore) scales with the lateral size of the array. We account for the variation in pore size diameter by scaling the contribution of each pore by its area. We arrive at:

$$\gamma_{eff} \approx \sum_i \sqrt{\frac{d_i^2}{d_{avg}^2}} \quad (7)$$

Noting that the second term in the parentheses of Eq. (5) accounts for access resistance, we can combine Eq. (5) and (6) to arrive at an approximate relationship between the conductance and pore size distribution for a tightly packed and large array of heterogeneous pores:

$$G = \sum_i G_i \approx \sum_i k_b \left( \frac{4L}{\pi d_i^2} \frac{1}{1 + 4 \frac{l_{Du}}{d_i}} + \frac{1}{d_{eff,i} + l_{Du}} \right)^{-1},$$

$$d_{eff,i} \approx \frac{d_i}{1 + \gamma_{eff} \frac{d_i}{2L}} \quad (8)$$

## Supplementary References

1. Liu, Y. *et al.* Layer-by-layer thinning of MoS<sub>2</sub> by plasma. *ACS Nano* **7**, 4202–4209 (2013).
2. Nečas, D. & Klapetek, P. Gwyddion: an open-source software for SPM data analysis. *Open Physics* **10**, 181–188 (2012).
3. Yagasaki, T., Matsumoto, M. & Tanaka, H. Lennard-Jones Parameters Determined to Reproduce the Solubility of NaCl and KCl in SPC/E, TIP3P, and TIP4P/2005 Water. *J. Chem. Theory Comput.* **16**, 2460–2473 (2020).
4. Bock, C. W., Kaufman, A. & Glusker, J. P. Coordination of water to magnesium cations. *Inorg. Chem.* **33**, 419–427 (1994).
5. Tsimpanogiannis, I. N. *et al.* Self-diffusion coefficient of bulk and confined water: a critical review of classical molecular simulation studies. *Molecular Simulation* **45**, 425–453 (2019).
6. Liu, G. *et al.* Eliminating lattice defects in metal–organic framework molecular-sieving membranes. *Nature Materials* (2023) doi:10.1038/s41563-023-01541-0.
7. Lu, J. *et al.* Efficient metal ion sieving in rectifying subnanochannels enabled by metal–organic frameworks. *Nature Materials* **19**, 767–774 (2020).
8. Xu, T. *et al.* Engineering leaf-like UiO-66-SO<sub>3</sub>H membranes for selective transport of cations. *Nano-Micro Letters* **12**, 51 (2020).
9. Gao, L., Chan, K.-Y., Li, C.-Y. V., Xie, L. & Olorunyomi, J. F. Highly selective transport of alkali metal ions by nanochannels of polyelectrolyte threaded MIL-53 metal organic framework. *Nano Lett.* **19**, 4990–4996 (2019).
10. Lu, J. *et al.* Ultrasensitive monovalent metal ion conduction in a three-dimensional sub-1 nm nanofluidic device constructed by metal–organic frameworks. *ACS Nano* **15**, 1240–1249 (2021).
11. Abraham, J. *et al.* Tunable sieving of ions using graphene oxide membranes. *Nature Nanotechnology* **12**, 546–550 (2017).
12. Esfandiari, A. *et al.* Size effect in ion transport through angstrom-scale slits. *Science* **358**, 511–513 (2017).
13. Hirunpinyopas, W., Prestat, E., Iamprasertkun, P., Bissett, M. A. & Dryfe, R. A. W. Potential dependent ionic sieving through functionalized laminar MoS<sub>2</sub> membranes. *2D Materials* **7**, 015030 (2019).
14. Xi, Y.-H. *et al.* Graphene-based membranes with uniform 2D nanochannels for precise sieving of mono-/multi-valent metal ions. *Journal of Membrane Science* **550**, 208–218 (2018).
15. Song, J., Yu, H.-W., Ham, M.-H. & Kim, I. S. Tunable ion sieving of graphene membranes through the control of nitrogen-bonding configuration. *Nano Lett.* **18**, 5506–5513 (2018).
16. Fu, Y. *et al.* Dehydration-determined ion selectivity of graphene subnanopores. *ACS Appl. Mater. Interfaces* **12**, 24281–24288 (2020).
17. Jain, T. *et al.* Heterogeneous sub-continuum ionic transport in statistically isolated graphene nanopores. *Nature Nanotechnology* **10**, 1053–1057 (2015).
18. Feng, J. *et al.* Observation of ionic Coulomb blockade in nanopores. *Nature Materials* **15**, 850–855 (2016).
19. Thiruraman, J. P., Masih Das, P. & Drndić, M. Stochastic ionic transport in single atomic zero-dimensional pores. *ACS Nano* **14**, 11831–11845 (2020).
20. Rollings, R. C., Kuan, A. T. & Golovchenko, J. A. Ion selectivity of graphene nanopores. *Nature Communications* **7**, 11408 (2016).
21. Su, S. *et al.* Multifunctional graphene heterogeneous nanochannel with voltage-tunable ion selectivity. *Nature Communications* **13**, 4894 (2022).



22. Wyss, R. M., Tian, T., Yazda, K., Park, H. G. & Shih, C.-J. Macroscopic salt rejection through electrostatically gated nanoporous graphene. *Nano Lett.* **19**, 6400–6409 (2019).
23. Robin, P., Kavokine, N. & Bocquet, L. Modeling of emergent memory and voltage spiking in ionic transport through angstrom-scale slits. *Science* **373**, 687–691 (2021).
24. Fyta, M. & Netz, R. R. Ionic force field optimization based on single-ion and ion-pair solvation properties: Going beyond standard mixing rules. *J. Chem. Phys.* **136**, 124103 (2012).
25. Ganguly, P., Hajari, T. & van der Vegt, N. F. A. Molecular Simulation Study on Hofmeister Cations and the Aqueous Solubility of Benzene. *J. Phys. Chem. B* **118**, 5331–5339 (2014).
26. Dang, L. X. Mechanism and thermodynamics of ion selectivity in aqueous solutions of 18-crown-6 ether. A molecular dynamics study. *Journal of the American Chemical Society* **117**, (1995).
27. Mamatkulov, S., Fyta, M. & Netz, R. R. Force fields for divalent cations based on single-ion and ion-pair properties. *J. Chem. Phys.* **138**, 024505 (2013).
28. Kozbial, A., Gong, X., Liu, H. & Li, L. Understanding the Intrinsic Water Wettability of Molybdenum Disulfide (MoS<sub>2</sub>). *Langmuir* **31**, 8429–8435 (2015).
29. Storey, B. D. & Bazant, M. Z. Effects of electrostatic correlations on electrokinetic phenomena. *Phys. Rev. E* **86**, 056303 (2012).
30. Allen, M. P. & Tildesley, D. J. *Computer Simulation of Liquids*. (Oxford University Press, 2017). doi:10.1093/oso/9780198803195.001.0001.
31. Ryckaert, J.-P., Ciccotti, G. & Berendsen, H. J. C. Numerical integration of the cartesian equations of motion of a system with constraints: molecular dynamics of n-alkanes. *Journal of Computational Physics* **23**, 327–341 (1977).
32. Feng, J. *et al.* Single-layer MoS<sub>2</sub> nanopores as nanopower generators. *Nature* **536**, 197–200 (2016).
33. Plimpton, S. Fast parallel algorithms for short-range molecular dynamics. *Journal of Computational Physics* **117**, 1–19 (1995).
34. Martínez, L., Andrade, R., Birgin, E. G. & Martínez, J. M. PACKMOL: A package for building initial configurations for molecular dynamics simulations. *Journal of Computational Chemistry* **30**, 2157–2164 (2009).
35. Kohlmeyer, A. & Vermaas, J. TopoTools: release 1.9. (2022).
36. Michaud-Agrawal, N., Denning, E. J., Woolf, T. B. & Beckstein, O. MDAAnalysis: A toolkit for the analysis of molecular dynamics simulations. *Journal of Computational Chemistry* **32**, 2319–2327 (2011).
37. Perram, J. W. & Stiles, P. J. On the nature of liquid junction and membrane potentials. *Phys. Chem. Chem. Phys.* **8**, 4200–4213 (2006).
38. Gadaleta, A. *et al.* Sub-additive ionic transport across arrays of solid-state nanopores. *Physics of Fluids* **26**, 012005 (2014).
39. Lee, C. *et al.* Large apparent electric size of solid-state nanopores due to spatially extended surface conduction. *Nano Lett.* **12**, 4037–4044 (2012).